JGR Atmospheres

RESEARCH ARTICLE
10.1029/2021JD035343

Intra-Annual Variation of Eddy Diffusion (k_{zz}) in the MLT, From SABER and SCIAMACHY Atomic Oxygen Climatologies

G. R. Swenson[1], F. Vargas[1], M. Jones[2], Y. Zhu[3], M. Kaufmann[4,5], J. H. Yee[6], and M. Mlynczak[7]

[1]Department of Electrical and Computer Engineering, University of Illinois, Urbana, IL, USA, [2]Space Science Division, U.S. Naval Research Laboratory, Washington, DC, USA, [3]National Space Science Center, Chinese Academy of Sciences, Beijing, China, [4]Institute of Energy and Climate Research (IEK-7), Forschungzentrum Juelich GmbH, Juelich, Germany, [5]Department of Physics, University of Wuppertal, Wuppertal, Germany, [6]Applied Physics Laboratory, The Johns Hopkins University, Baltimore, MD, USA, [7]NASA, Langley Research Center, Hampton, VG, USA

Abstract Atomic oxygen (O) in the mesosphere and lower thermosphere (MLT) results from a balance between production via photo-dissociation in the lower thermosphere and chemical loss by recombination in the upper mesosphere. The transport of O downward from the lower thermosphere into the mesosphere is preferentially driven by the eddy diffusion process that results from dissipating gravity waves and instabilities. The motivation here is to probe the intra-annual variability of the eddy diffusion coefficient (k_{zz}) and eddy velocity in the MLT based on the climatology of the region, initially accomplished by Garcia and Solomon (1985, https://doi.org/10.1029/JD090iD02p03850). In the current study, the intra-annual cycle was divided into 26 two-week periods for each of three zones: the northern hemisphere (NH), southern hemisphere (SH), and equatorial (EQ). Both 16 years of SABER (2002–2018) and 10 years of SCIAMACHY (2002–2012) O density measurements, along with NRLMSIS® 2.0 were used for calculation of atomic oxygen eddy diffusion velocities and fluxes. Our prominent findings include a dominant annual oscillation below 87 km in the NH and SH zones, with a factor of 3–4 variation between winter and summer at 83 km, and a dominant semiannual oscillation at all altitudes in the EQ zone. The measured global average k_{zz} at 96 km lacks the intra-annual variability of upper atmosphere density data deduced by Qian et al. (2009, https://doi.org/10.1029/2008JA013643). The very large seasonal (and hemispherical) variations in k_{zz} and O densities are important to separate and isolate in satellite analysis and to incorporate in MLT models.

Key Points:

- Intra-annual variations (IAVs) of k_{zz} in the MLT, from SABER and SCIAMACHY atomic oxygen climatologies are determined
- Deduced k_{zz} values at mid-latitudes have a prominent annual oscillation below 87 km, while equatorial values vary semiannually (80–96 km)
- Hemispherical IAVs (seasonal) in k_{zz} and O density dominate the MLT, contrary to the global averages used currently in some GCMs

Correspondence to:

G. R. Swenson,
swenson1@illinois.edu

Citation:

Swenson, G. R., Vargas, F., Jones, M., Zhu, Y., Kaufmann, M., Yee, J. H., & Mlynczak, M. (2021). Intra-annual variation of eddy diffusion (k_{zz}) in the MLT, from SABER and SCIAMACHY atomic oxygen climatologies. *Journal of Geophysical Research: Atmospheres*, *126*, e2021JD035343. https://doi.org/10.1029/2021JD035343

Received 1 JUN 2021
Accepted 12 NOV 2021

Author Contributions:

Formal analysis: F. Vargas
Investigation: G. R. Swenson, M. Jones, Y. Zhu, M. Kaufmann, J. H. Yee, M. Mlynczak
Resources: M. Jones
Software: F. Vargas
Validation: F. Vargas
Writing – original draft: G. R. Swenson
Writing – review & editing: M. Jones, Y. Zhu, M. Kaufmann, J. H. Yee, M. Mlynczak

1. Introduction

The intra-annual variation of turbulent processes in the mesosphere and lower thermosphere (MLT) are important to the distribution of constituents both within and above this region, including atomic oxygen. Garcia and Solomon (1985) studied these very processes, with findings that have stood the test of time. Upward coupling of gravity waves from the lower atmosphere plays a key role in the vertical mixing and constituent distribution in the MLT. Turbulence is due to convective and shear instabilities, combined with dissipating gravity waves (Fritts & Alexander, 2003; Hines, 1960; Lübken, 1997), account for the majority of disturbances that result in eddy diffusion of constituents with respect to the background atmosphere (Becker & von Savigny, 2010; Gardner, 2018; Swenson et al., 2018). Eddy diffusion constituent transport effects in the thermosphere-ionosphere-electrodynamics general circulation model by introducing a global average, intra-annual variable eddy diffusion coefficient at 97 km to couple MLT oxygen densities with the thermosphere (Qian et al., 2009, 2013). Another approach has been to propagate tropospheric originating gravity waves from below, via a mechanistic model of MLT composition (Becker & von Savigny, 2010; Becker et al., 2020; Grygalashvyly et al., 2012), and also by whole atmosphere community climate model (Garcia et al., 2007; Liu et al., 2018). Filtering gravity waves from below by stratospheric and mesospheric winds is an important aspect of the coupling. Parameterizing subgrid-scale phenomena in general circulation models is a difficult task, but finer grid resolution in the models of the middle and upper atmosphere are leading to improved representations of GWs in the MLT and overlying thermosphere (see Liu et al., 2018).

The climatological distributions of constituents in the MLT are influenced by the eddy transport processes which redistribute constituents both horizontally and vertically. One of the simplest to understand is the atomic oxygen

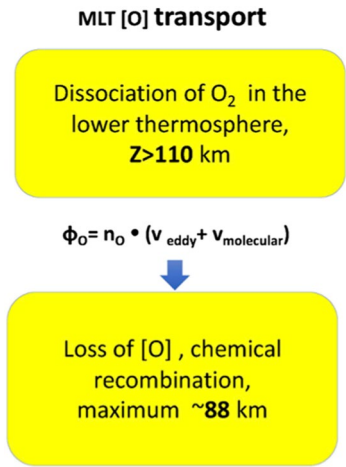

Figure 1. Mesosphere and lower thermosphere O transport schematic. Atomic oxygen is produced via photo-dissociation of O_2 and diffuses downward by both molecular and eddy processes to the mesosphere, where loss occurs through recombination (e.g., Colegrove et al., 1965, 1966).

distribution, initially characterized by Colegrove et al. (1965). Atomic oxygen is produced above ~100 km by photo-dissociation of O_2, and diffuses downward by eddy processes including turbulence and dissipating gravity waves (see Figure 1 schematics). The method of parameterized eddy diffusion velocity is determined by the loss chemistry of atomic oxygen, which recombines near 87 km. Swenson et al. (2018, 2019), hereafter S18 and S19, respectively, refined the method of Colegrove et al. (1966) to determine the global mean parameterized coefficient profile k_{zz} in the MLT, using measurements of OH airglow emissions from thermosphere ionosphere mesosphere energy and dynamics (TIMED) SABER (Mlynczak et al., 2013; Russell et al., 1999) over 16 years, as well as from the Envisat SCIAMACHY (Kaufmann et al., 2014; Zhu & Kaufmann, 2018) measurements of both OH and O(^{1}S) over 10 years.

This study is Part II of the S19 study, in which we extend our k_{zz} determination and analysis to examine intra-annual variations (IAVs) within three latitudinal zones: the northern hemisphere low-to-mid latitudes (NH, 15–55°), the southern hemisphere low-to-mid latitudes (SH, −15 to −55°), and equatorial latitudes (EQ, ±15°). The investigations are being implemented in a sequence, the intra-annual variation of bi-weekly zonal averages (IAVs), the global IAV (by area weighting the three zones), which are deviations from the global mean (see S19), and deserves a dedicated discussion. Intra-annual variations have been studied by Salinas et al. (2016) using SABER CO_2 measurements. Variations associated with thermospheric waves and advection have been described by Jones et al. (2014, 2017, 2018) where thermospheric O densities vary with an AO, we surmise to be driven by k_{zz}. This study specifically focuses on the IAV of k_{zz}, and additionally, the IAV of the MLT oxygen density, a parameter that varies separately with respect to the determination of the diffusive flux of O, in the MLT. We feel it is important to establish these basic coupling processes and that they are incorporated into models so that more complex issues of advection and circulation effects can be better analyzed and understood.

2. Method Summary and Discussion

The primary transport mechanism for O is diffusion, where the total diffusive flux (nv), and the diffusion velocity are the sum of the molecular and eddy components (Equation 1 below, see S19). The integral loss rate of O, via chemistry, is assumed to be supplied by the downward diffusive flux (Equation 2).

The method for the determination of k_{zz} is as follows. Equations 1 and 2 both describe the downward flux of atomic oxygen, where (a) is traditional composition relationships and (b) is driven by the O loss due to chemistry. The chemical processes are described in our previous two studies, S18 and S19. The chemistry in Equation 2 is described in S18, and the rate coefficients (k_1, k_4, and k_6) are from Sander et al. (2011). We begin the analysis by calculating the downward flux with Equation 2. The flux is then divided by the oxygen density for the determination of the total diffusion velocity versus altitude. Using Equation 3, the eddy diffusion velocity is determined by subtracting the molecular diffusion velocity. Finally, Equation 4, a variable component of Equation 1, is used to determine k_{zz}. k_{zz} is the parameterized eddy diffusion coefficient which represents the transport due to mixing from dissipating and breaking waves and instabilities.

The vertical eddy velocity is a function of the total density gradient imposed by the scale height, the atomic oxygen gradient, and the temperature gradient. On average, the O loss chemistry drives the slope of the oxygen density and bottom side (below 96 km) O profile. Vertical advection changes the vertical gradient of O, so k_{zz} is sensitive to vertical advection. Especially note the oxygen dependence in Equation 4 is via the gradient of O, which is insensitive to a change in the oxygen density, given changes in O density affect the numerator and denominator equally, resulting in a null effect on the k_{zz}. The previous studies (S19, S19) employing this methodology involved global, long term averaging of O profiles which also negate horizontal and vertical advection effects. In this study, we analyze and describe the uncertainties associated with advection processes on the results presented herein, both in Section 5.2) and in Appendix D.

$$\phi_O(z) = -D_i[O]\left(\frac{1}{H_i} + \frac{1}{T}\frac{dT}{dz} + \frac{1}{[O]}\frac{d[O]}{dz}\right) - k_{zz}[O]\left(\frac{1}{H} + \frac{1}{T}\frac{dT}{dz} + \frac{1}{[O]}\frac{d[O]}{dz}\right) \quad (1)$$

$$\phi_O(z) = \int_{z=80}^{z} (-2k_1[O][O_2][M] - 2k_4[O]^2[M] - 2k_6[H][O_2][M])\ dz' \quad (2)$$

$$v_{O,eddy}(z) = v_O(z) - v_{O,md}(z) \quad (3)$$

$$k_{zz} = -\frac{v_{O,eddy}}{\left(\frac{1}{H} + \frac{1}{T}\frac{dT}{dz} + \frac{1}{[O]}\frac{d[O]}{dz}\right)} \quad (4)$$

The term definitions for the equations are described in Appendix A.

Equation 2 used to calculate the integral loss rate, from 80 km to z, where z is the altitude for which a diffusion velocity is calculated, was similar to that described by S19, with one exception. S19 defined the OH loss process using:

$$O_3 + H \rightarrow OH^* + O_2, \qquad k_2 = 1.4 \times 10^{-10}\exp(-470/T) \quad (5)$$

where the global mean values of ozone and hydrogen density were used to determine the O loss rate. In this study, that expression was replaced with the reaction:

$$O + O_2 + M \rightarrow O_3 + M, \qquad k_1 = 6.4 \times 10^{-34}(300/T)^{2.4}, (Sander\ \ etal.,) \quad (6)$$

where M is molecular density, $N_2 + O_2$. Equation 6 is the unique source of the ozone in Equation 5, enabling the study to directly incorporate SABER and SCIAMACHY atomic oxygen effects on k_{zz}. A detailed discussion and references regarding the O recombination (Equation 6) result in ozone formation, and at nighttime results in the excited OH emission was provided by these authors in Section 2.1 of S19. The O density and reaction coefficients for the loss rate are unique for each of the 78 temporal/spatial elements. The second and third terms in Equation 2 are described in Appendix A, where the definition of altitude is geometric.

The integral flux in Equation 2 is an upper limit since some O is produced via pre-dissociation in the mesosphere by the Schumann-Runge bands (e.g., Frederick & Hudson, 1980). We computed the average hemispherical production rate from the Schumann-Runge bands (S-R bands) in the 85–92 km altitude region in Figure 7 of Koppers and Murtagh (1996) to be 8.5×10^4 cm^{-3}s^{-1} for the overhead sun, and the average nighttime, the hemispherical O loss rate is 1.5×10^6 cm^{-3}s^{-1}. The ratio is 5.6% for the overhead sun, but the average dayside production rate would be or ~1/2 this value. We are performing a detailed study of O production and loss continuity that will refine this fraction, but the relative intra-annual variabilities of k_{zz} are unaffected. The k_{zz} values calculated herein, are an upper limit where the values are less by the fraction of O produced locally by the S-R bands. This fraction is comparable to the fraction determined from the Frederick and Hudson (1980) model values used by S19, where a comparable fraction was calculated.

3. Data and Analysis

The effects of tidal and planetary waves are minimized by averaging. The sample averages of both SABER and SCIAMACHY data were chosen to be 14 days for 10 years of SCIAMACHY data and 16 years of SABER data. The spatial zones are large which minimizes coupling by advection from adjacent spatial/temporal domains.

The three zones (NH, SH, and EQ) were combined with the 26 two week periods to describe the intra-annual cycle, a total of 78 temporal/spatial elements for analysis. In addition to the observed SABER and SCIAMACHY O profiles, N_2, O_2, H, and neutral temperatures must be determined for each of the 78 elements. N_2, O_2, H, and neutral temperatures were computed using NRLMSIS 2.0, MSIS2.0 (Emmert et al., 2021), for each of the 78 elements. The model has recently been upgraded to include a large amount of available satellite and ground based data over the past 20 years. Both SCIAMACHY (2002–2012) and SABER (2002–2018) covered a solar cycle, whose minimum was 2008. We chose an average F10.7 value for the 2002–2012 as a mean value for the model computations. Note that over the solar cycle, there is very little variation of the constituents or temperature at the MLT altitudes (80–105 km), where the k_{zz} values are being computed. For equatorial conditions, MSIS

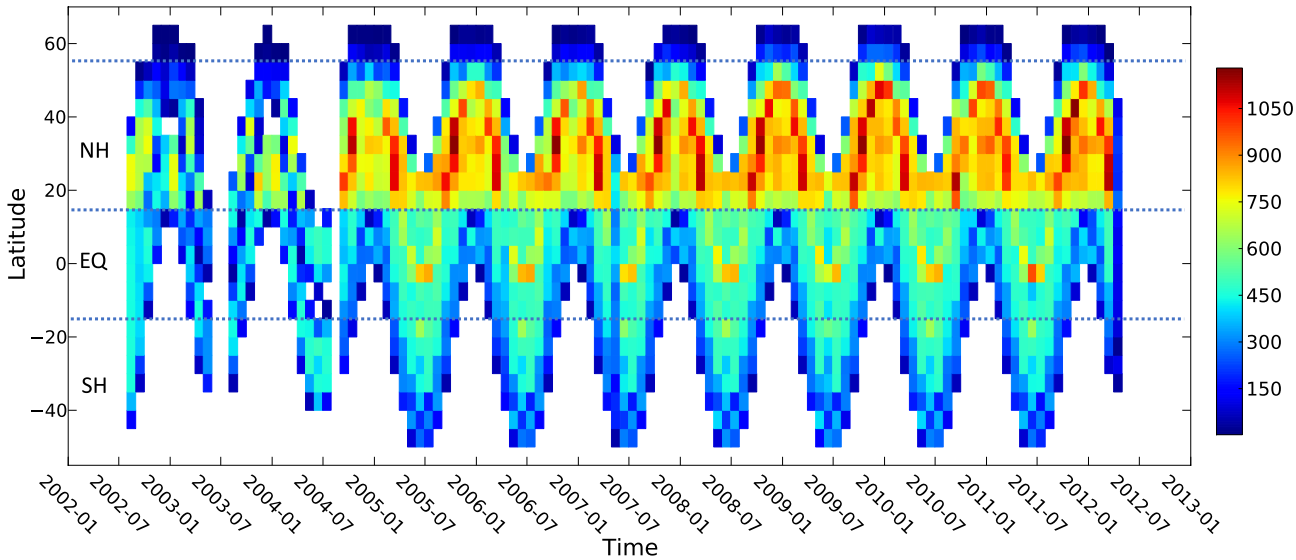

Figure 2. A plot of sampling statistics for SCIAMACHY nighttime measurements, for latitude versus time (2002–2012). The dotted horizontal lines define the limits of the zonal boundaries within which the zonal data were analyzed. There are significant data gaps in the summer for all zones (northern hemisphere, southern hemisphere [SH], equatorial), and at lower latitudes (<−40°) in the SH.

determination of changes of 100 $F_{10.7}$ units resulted in <1% change in N_2 density and *T*, and 11% change in O density. The change in O density is consistent with the change in the FUV flux associated with the Schumann-Runge spectral region and the O_2 pre-dissociation rate (see Lednyts'kyy et al., 2017). The S18 study found negligible inter-annual variation in k_{zz} with the exception of the QBO (Quasi-biannual oscillation) in the EQ region. The NRLMSIS 2.0 model calculations were made for the respective day of the year for a given period, and the spatial location chosen was −40° latitude for the SH, 0° latitude for the EQ, and +40° latitude for the NH, where the chosen values were representative for the zones.

There is a significant spatial and temporal pattern in the SCIAMACHY data base. The sampling frequency versus latitude and time is plotted in Figure 2. There was some sampling bias in the first 2 years of operation (2002–2004) where sampling at all eligible times was under-sampled relative to later years. The missing data after 2004 is mainly owing to (a) solar irradiance measurements, (b) spectral calibration, (c) relative radiometric calibration, and (d) dark current measurements. In addition to the above calibration measurements, quote "The ENVISAT orbit solar occultation was restricted to latitudes between 65°N and 90°N. The lunar occultation was performed from half moon to full moon. For periods of 5–8 days per month lunar occultation measurements provided latitudinal coverage from 30 to 90S. The solar scanning strategy is similar to the SAGE II scanning (Mauldin III et al., 1985): during sunrise, SCIAMACHY scans several times over the full solar disc" Bovensmann et al. (1999). SCIAMACHY data is plotted where the signal is large enough the signal-noise provides a minimal error to the measurement. Note that SCIAMACHY provides data for both OH (80–96 km) and O(^{1}S, 557.7 nm), (88–105 km). In this study, it was required that both emissions were measured for a given 2-week period. Additionally, the SCIAMACHY data were not used to compute zonally (i.e., NH, SH, or EQ zones) nor global average results, but it is plotted for respective intra-annual variations within a zone, for relevant seasonal information.

The TIMED satellite inclination is 74°. The satellite was maneuvered through a yaw cycle every 60 days, at approximately the same day each year, to orient the SABER instrument to view in the anti-sunward direction. The intent was for SABER to yaw on the same days each year, but over time, the satellite altitude has dropped at the rate of about 1 km per year. The inclination of the orbit has not changed. However, the effect of the altitude decrease is for the yaw dates to creep earlier than their original dates. For example, the first yaw of the year used to occur on January 22. That same yaw now occurs in late December. The yaw maneuver, as well as the TIMED orbit geometry, enabled the SABER instrument to acquire data on all days of the year, unlike the SCIAMACHY data described in the previous paragraph. The latitudinal coverage has a sampling bias, sampling further southward in a given cycle, and alternately northward bias in the subsequent cycle. The number of measurements at all latitudes between ±55° is large for all years for the 2 week sampling performed herein. Within a given 60 days

yaw orientation, there is a variation in the local time of night sampled through the cycle. The amplitude of O density variation is discussed in the data analysis section that follows.

Equation 1 lacks advection terms (Gardner, 2018), an assumption implying turbulence and wave processes uniquely and solely describe the vertical O distribution. The vertical distribution of O is driven by the downward flux of O, via the diffusion velocity (k_{zz}), as well as advection. Our prior analysis (S18, S19) involved calculations of globally averaged k_{zz}. In those studies, the global average constituent profiles for all latitudes were averaged for a minimum of a year (S18). As a result, any advection contribution was arguably minimized through long-term averaging. Advection potentially influences the O density from an adjacent zone. It was pointed out in the previous section that k_{zz} and the O density are treated as separate variables. k_{zz} (driven by the vertical gradient of O) and O density (where horizontal distributions are potentially influenced by advection) are separate. The separation of variables in the intra-annual cycle (k_{zz} and [O]) is critical to establishing the vertical coupling of constituents in the MLT.

The 14-day interval was chosen with the rationale that follows. Diffusion times are an important consideration. Considering a breaking wave condition in the layer and an anomaly in the altitude distribution is redistributed over altitude by diffusion in time. Lednyts'kyy et al. (2017) measured the time delay from the solar variation in the 27-day rotation (and associated photo-dissociation of O_2) to the time the variation appears in the O(^{1}S) emission near 95 km, to be ∼13 days. It is estimated that it takes an additional week to diffusively transport O from 95 to 87 km, the altitude of maximum loss via recombination (S19). Consequently, sampling average composition distributions at a temporal resolution shorter than 2 weeks would potentially, fail to reach an equilibrium condition. This criterion is overstated considering averaging for 16 years. A statistically significant number of measurements is also necessary, clearly evident in Figure 2 for SCIAMACHY. Twenty six 2-week periods constitute the data elements for the analysis of intra-annual variability, for each of the three latitudinal zones.

The O density from both the SABER and SCIAMACHY data archives were computed for each of the elements for each year available (16 years for SABER and 10 years for SCIAMACHY) and averaged for all the years. As a result, the k_{zz} determined for each of the elements represents the climatological mean for that element.

4. Results

Results for the average time evolution of k_{zz} and a 2-D (day of year vs. altitude) variation of amplitude for 16 years of SABER data are illustrated in Figures 3a–3e and Figures 3b–3f, respectively. Tables of values of k_{zz} for Figures 3b, 3d, and 3f are provided in Appendix C. The SCIAMACHY data were not included in this initial analysis due to the sampling biases described above. The 2-D plot illustrates the dominant periods being an AO, in both the NH and SH below 87 km, and the SAO at EQ at all altitudes consistent with the latitudinal variability in IAVs of received solar radiation and surface temperature (see Picone et al., 2019), as well as observed and model IAVs in k_{zz} and middle atmospheric winds by Garcia and Solomon (1985) and Garcia et al. (1997). The amplitude of the EQ SAO in spring is larger than in the fall. The lack of variability with altitude in k_{zz} for the EQ versus the NH/SH is unexpected. The details of the intra-annual AO and SAO variations for the respective zones are described in detail in the following subsections.

4.1. Northern and Southern Hemisphere and the AO

The results for the NH low-to-mid-latitude region are shown for SABER in Figure 4a. The most prominent IAV depicted at the four altitudes (96, 91, 87, and 83 km) is the AO, below 87 km, with a maximum in the middle of the summer, and a minimum in winter. We also note that there is minimal variation in k_{zz} above 87 km, including the upper limit of SABER data, at 96 km. Figures 4b and 4c are plots of k_{zz} for both SABER and SCIAMACHY data for 83 and 96 km, respectively. Some SCIAMACHY data is missing in mid summer, but with the data available, the suggestion is the amplitude at 83 km of the summer AO maximum may be slightly less than that for SABER (Figure 4b). Figure 4c illustrates there is little IAV at 96 km in both SABER and SCIAMACHY. There appears to be a minor peak near the summer solstice in both SABER and SCIAMACHY.

The AO of k_{zz} is the dominant oscillation in both SABER and data for the SH (Figures 5a and 5b) and SCIAMACHY for the winter, in b. The altitude of most variability is below 89 km increasing to the lower limit near 80 km (Figures 3b and 3f). The variabilities are a maximum near the summer solstice and a minimum in the

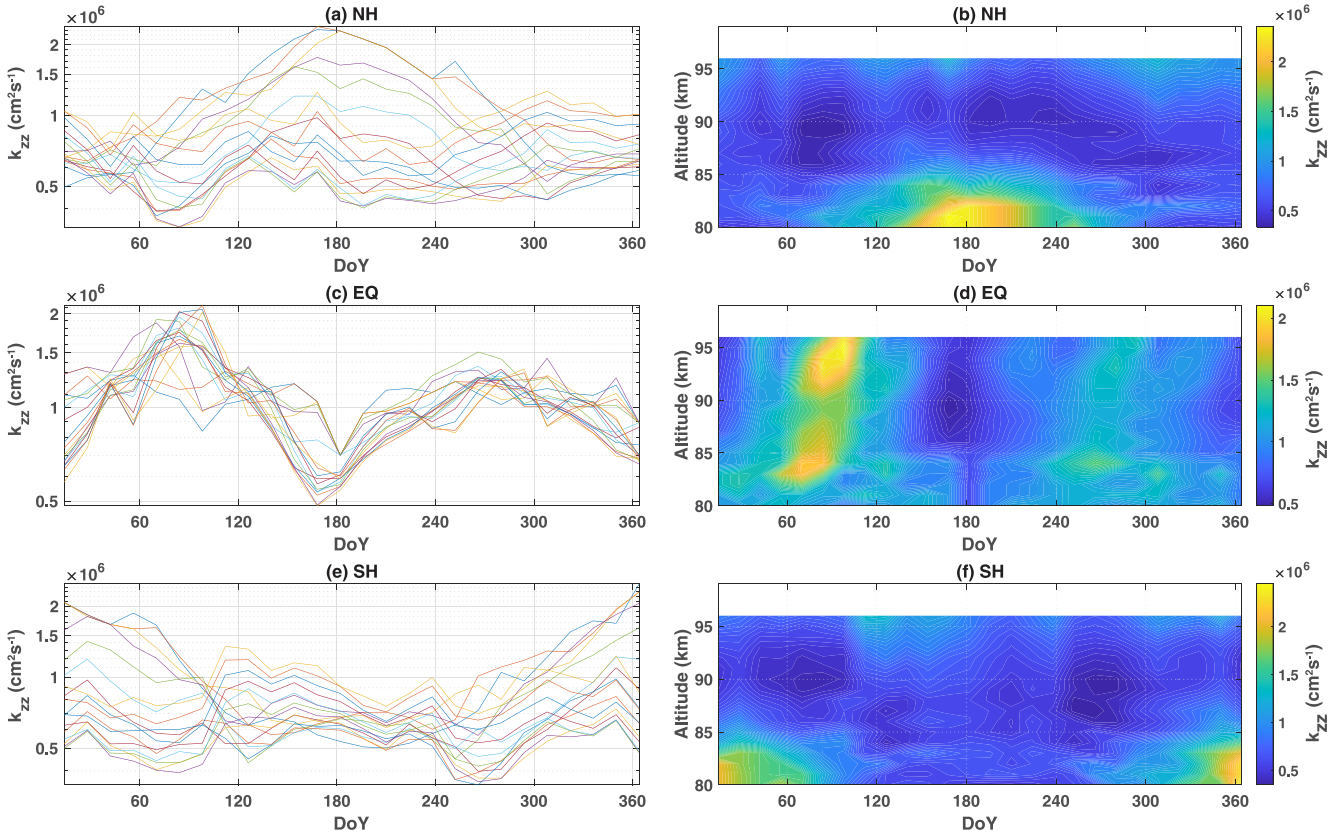

Figure 3. (a), (c), (e) Variation of k_{zz} deduced from SABER measurements, with the day of year in the northern hemisphere (NH), equatorial (EQ), and southern hemisphere (SH) latitude bands. Each colored line represents a different altitude in the range of 80–100 km. (b), (d), (f) Variation of k_{zz} with day of year and altitude is shown for the NH, EQ, and SH latitude bands.

winter (near the solstice). The amplitude of the winter to summer k_{zz} at 83 km changes by a factor of ~4 (see 3b). The SCIAMACHY and SABER k_{zz} are nearly equal for the winter, where SCIAMACHY data was available, with a hint of winter to summer transition at day 110. A clear 180 days phase shift in the AO is evident (Figure 5b), clearly associated with the season.

k_{zz} as a function of altitude calculated from SABER and SCIAMACHY O measurements, for the NH summer maximum versus winter minimum is shown in Figure 6. SCIAMACHY on Envisat is in a 10 a.m./p.m. polar orbit. The sampling pattern is the result of the requirement that the full line-of-sight of SCIAMACHY shall be in complete darkness and that some calibration measurements are performed in the southern hemisphere during nighttime, resulting in fewer data points in the SH compared to the NH. The data chosen for this figure was for periods 26 (end of year) and 1 (beginning of year) for the winter profile, and period 12 (early June) for the summer values. SABER winter was the same as SCIAMACHY, but the summer was period 13 and 14 (late June and early July), chosen for its availability at the summer solstice. The k_{zz} plots for both SABER and SCIAMACHY illustrate similar variations, below 90 km, with maximum to the lower limit of the data at 80 km. The NH is plotted since SCIAMACHY has data for both winter and summer for this comparison of k_{zz}. The large k_{zz} at the 80 km limit of sensing from SABER CO_2 in S19, was a result following the original analysis by Salinas et al. (2016). The integrated loss of O was integrated for the summer versus winter for a difference of 20% in the flux at 96 km, for those two extremes. The discussion relevant to these changes follows in the next two paragraphs.

Figure 7a is a plot of the intra-annual variation of k_{zz} at 96 km for the NH and similarly, Figure 7b for O density. The major variation in the O density is a broad peak near the summer solstice. In Figures 7a and 7b, the dates the satellite performed a yaw maneuver every 60 days, directs the SABER viewing direction to be anti-sunward with respect to the orbital plane. This yaw oscillation (YO) performed nearly the same day each year, is directly correlated to the same periodic brightness variation in the O density (Figure 7b). In each yaw cycle, the local hour

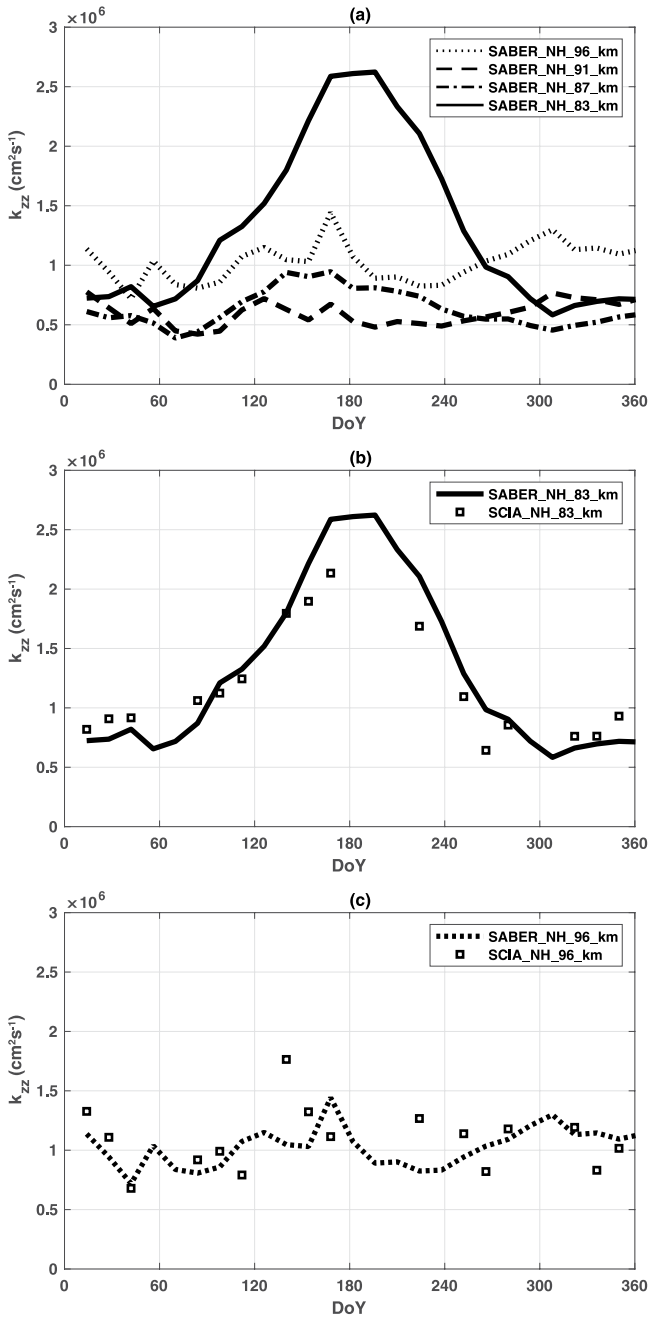

Figure 4. k_{zz} versus DoY for the NH. (a) Values determined from SABER O, for 96, 91, 89, and 83 km. The AO dominates at 83 km, driven by the meteorology from below, with a maximum in the summer. (b) Same as (a) except 83 km, for SABER (solid) and SCIAMACHY (dots). (c) Same as (b) except for 96 km.

sampled changes from the beginning to the end of the cycle, and consequently, brightness variations associated with local time variation contribute to the cycle in O density. There is variability in k_{zz} (Figure 7a) also, but not directly correlated since the O density has a negligible effect on k_{zz}. There is one event marked P2 in O density near DoY 170, and a spike in k_{zz} correlates with the sharp trough, following P2 in O density, which will be described in the discussion section. This event is not just a YO, but rather an event observed by both SABER and SCIAMACHY.

The next step in our analysis is to better understand the continuity and downward O flux in context with the AO and summer enhancement in O at 96 km, and the k_{zz} enhancement below 87 km. The variability of atomic oxygen flux at 96 km has been calculated for the NH and is plotted in Figure 8. The eddy diffusion velocity was determined for the same method used to determine k_{zz} in Figure 7a was multiplied by the O density (Figure 7b) for the calculation of the flux for Figure 8. An amplitude arrow of 10% (or minimum to maximum of 20%) is indicated in the figure. There is general consistency with the integral loss of O below 90 km, where there is a maximum at the summer solstice and a significantly lower flux in winter.

4.2. Equatorial Region and the SAO

A semiannual oscillation in k_{zz} is clearly evident at the EQ, with a much smaller AO than at low-to-mid latitudes (Figure 9). Note the SAO dominates at all altitudes, with a minimum SAO amplitude at 83 km. The amplitude of k_{zz} at 87 km and above varies between a summer solstice minimum and spring equinox by a factor of ~2, and from the summer solstice to the fall equinox by a factor of ~1.5. An observation in the phase shift in the SAO was noted in the spring when the amplitude is largest. The phase propagates upward near spring equinox from day 65 at 83 km to day 100 at 96 km.

4.3. Zonal k_{zz} and O Density IAVs

Figure 10 is a plot of the average k_{zz} versus altitude for the NH, SH, and EQ zones using SABER data. Note the NH and SH profiles are almost identical with altitude. Also noted is the near-constant distribution with altitude at the EQ zone.

We hypothesize this is likely due to a difference in the sources contributing to k_{zz}, both damped gravity waves and instabilities. Details of the rationale are described in the Section 5.

Figure 11 is a series of plots of the IAV associated with SABER O density. Figures 11a–11c are the IAVs of the percentage of O density change with altitude with respect to the global average density profile. Figures 11g and 11h describe the density IAV of O density at 96 and 85 km, respectively. The phase shift of the AO at the NH and SH with the season as well as the large SAO at the EQ region at 85 km are dominant features. It is noted in particular that the amplitude of the O density below 87 km is 180° out of phase with k_{zz}, suggesting the large values of downward diffusion velocity in the summer depletes the O. On the contrary, in the EQ zone, the fact that the enhanced k_{zz} (and diffusion velocity) is larger at all altitudes, the larger O densities near the altitude of maximum density (96 km), supplies the O density from above, overcoming the O-losses at lower altitude. This is a major difference between the influence of k_{zz} in the mid-latitudes and the AO effect in both hemispheres, to that of the SAO in the equatorial region.

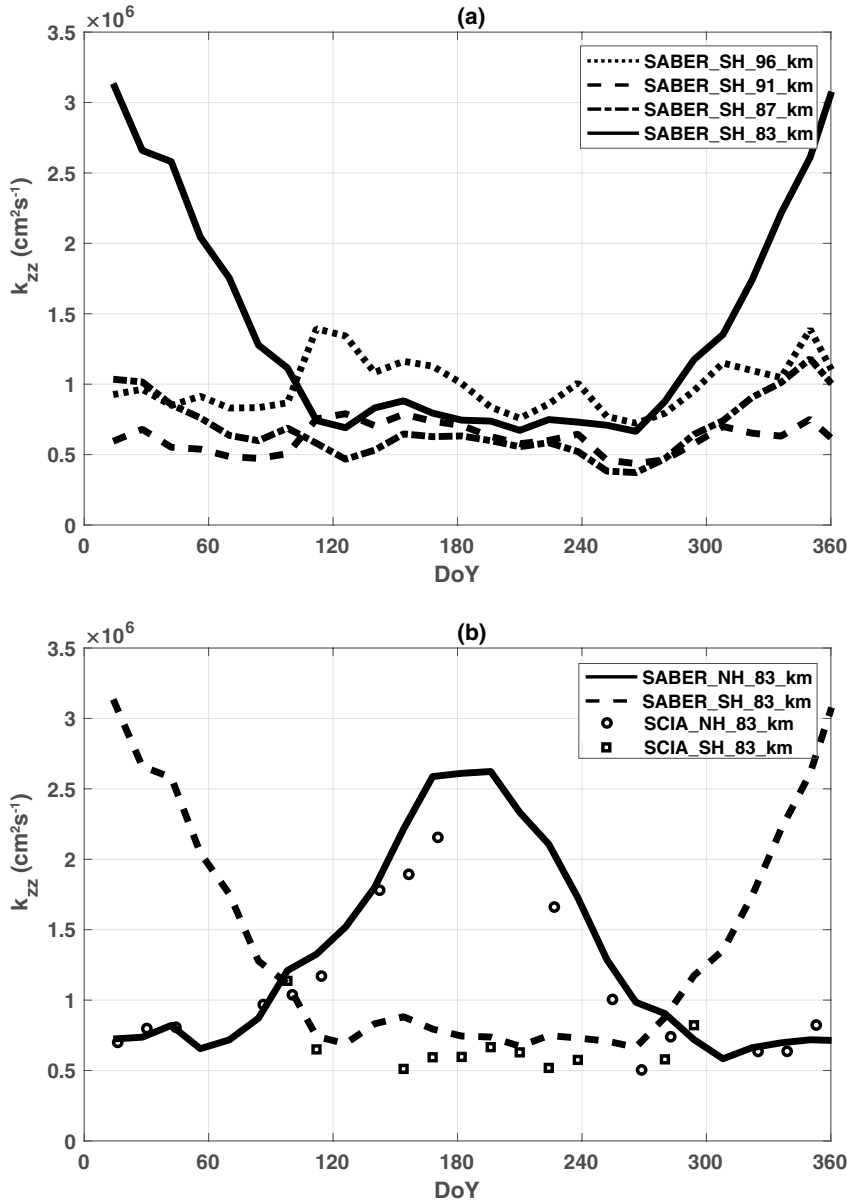

Figure 5. (a) Same as Figure 4a, except for the SH zone. (b) SABER southern hemisphere (SH) and northern hemisphere (NH), and SCIAMACHY SH and NH at 83 km.

4.4. Late Spring Event (NH, P2)

A large spike in O density and k_{zz} in the NH occurs in the spring in the SABER data shown in Figures 7b, 11a, and 11c, which is also present in the SCIAMACHY O density. Examination of a large amplitude at 96 km is noted with a peak at DoY 150 and a minimum (trough) at DoY 170 in the O density. Note the large peak in k_{zz} (Figure 7a) coincides with the trough in the O density (Figure 11b) where it has been highlighted with a dashed line (phase progressing upward). The feature is also apparent in the SH, shifted by 180 days.

The NH O density at 85 km versus DoY is shown in Figure 12. Considering the local time spread of the measurements over the SABER night which for 'night' consists of local times where the SZA > 95° (solar zenith angle, solid line). It was noted, that when the local time hour intervals are made smaller, the amplitude of the Spring event changes, illustrated in this case, for SZA > 130° (dotted line). The SABER data has a local time bias associated with the yaw periods (60 days), where the local time sampled shifts in local time from the beginning to the end of the

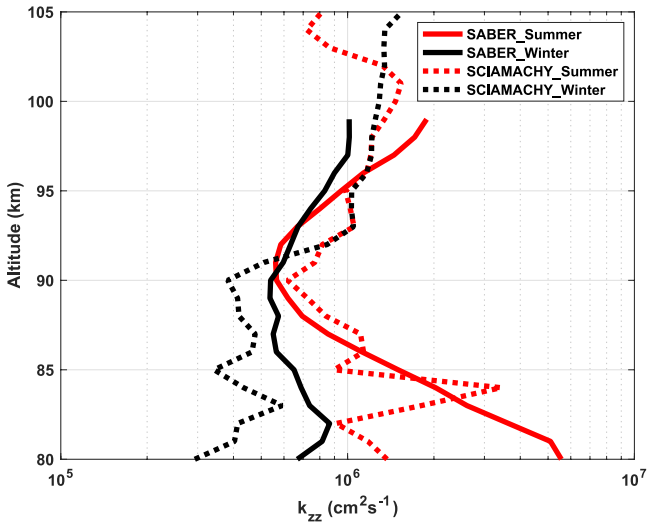

Figure 6. k_{zz} versus altitude for the northern hemisphere summer maximum (at summer solstice) and winter minimum (at winter solstice), for SABER and SCIAMACHY. The variability begins near 90 km, increasing with decreasing altitude. The variation between summer and winter is factor of ~4X for both O climatologies at 83 km.

yaw period. Studies of tidal influence on the mid-latitudes have recently been demonstrated by Tian et al. (2021), where meteor wind climatology observed the diurnal variability as well as IAV tidal effects on momentum fluxes associated with damped AGWs. We believe the change in amplitude of this spectral feature is due to filtering by the tides. The SCIAMACHY O data is also plotted as squares, which describes the same Spring event feature, where dashes highlight the specific feature amplitude. The SCIAMACHY data has gaps (shown as straight lines). Note that SCIAMACHY is always sampling at 10 p.m. local time. It is also important to note that the O densities are relatively small at 85 km, whereas the fractional changes due to the AO are large.

We hypothesize this Spring event may be a brief, vertical extension of the AO in k_{zz}. The specific source of the effect at higher altitude could be a result of an increase in the source amplitude in the troposphere and/or a change in the integral dynamical filtering effects which primarily occur in the stratosphere. We also note the slope with an altitude of the O density enhancement, is similar to the slope of the EQ k_{zz} at the spring equinox (SAO). It is plausible the event is a brief, very large excursion of a single or few years. Given the fact the oscillation appears in both SABER and SCIAMACHY data (Figure 12), those years would necessarily be between 2002 and 2012 when both SABER and SCIAMACHY were operating. We examined the O density for extreme outliers as well as the standard deviation of SABER O density. The O density (10^{11} cm^3 for the NH period 12 prior to 2012 (1.11, 1.64, 1.65) versus the entire sample (1.29, 1.62, 1.53) at 92, 94, and 96 km, respectively. There was no appreciable difference noted for a given year. We conclude that oscillation is an annual geophysical feature.

4.5. Global Average k_{zz} IAV

Global average (i.e., between ±55°) of SABER O density and k_{zz} as a function of day of the year at 96 km is shown in Figure 13a. The 96 km altitude was chosen because (a) it is the highest altitude of O resulting from OH airglow inversions used by SABER with relevant to global means, (b) is near 97 km chosen by (Qian et al., 2009) and (Salinas et al., 2016) intra-annual variation of k_{zz}, studies that are compared to later herein, and (c) it is representative of the altitude of maximum O density contribution to the downward flux. The global average for both O density and k_{zz} is computed by area weighting each zone by its an effective fractional area (0.364 for NH and SH each, and 0.272 for EQ). The Global average IAV (Figure 7b) is dominated by an SAO, reflecting the large EQ SAO contribution to the average. The intra-annual values of SABER k_{zz} are also plotted in Figure 13b where it is compared with that of (Qian et al., 2009).

The global average values of k_{zz} versus altitude for SABER are plotted in Figure 14 and compared with the values from the study of global means by S19.

5. Discussion

The phase and a peak altitude of the AO are consistent with dissipating and breaking GWs, which propagate upward from the lower atmosphere during the eastward phase of the stratospheric circulation. Westward propagating, high-frequency waves are unfiltered during this eastward phase and propagate freely. This hypothesis is also consistent with the extended increase which begins and ends near spring and fall equinox; the times at which the stratospheric winds reverse. These results are consistent with the analysis by Garcia & Solomon (1985). Their analysis of O_3 observations and O shape profiles were key elements of their discoveries, which here are confirmed and refined upon with SABER and SCIAMACHY data. These results are generally consistent with predictions from theory (Hines, 1960). A. Z. Liu (2009) analyzed the annual variation of k_{zz} from lidar observations at 35°N (Starfire Optical Range), where the IAV exhibits a similar peak in amplitude in summer, but at slightly higher altitudes (~90 km). Enhanced GW activity at mid-latitudes was also observed by Gardner et al. (2011) and Gardner (2018). Meteor wind observations at mid-latitude (~40°N by Tian et al. (2021), clearly illustrate IAV

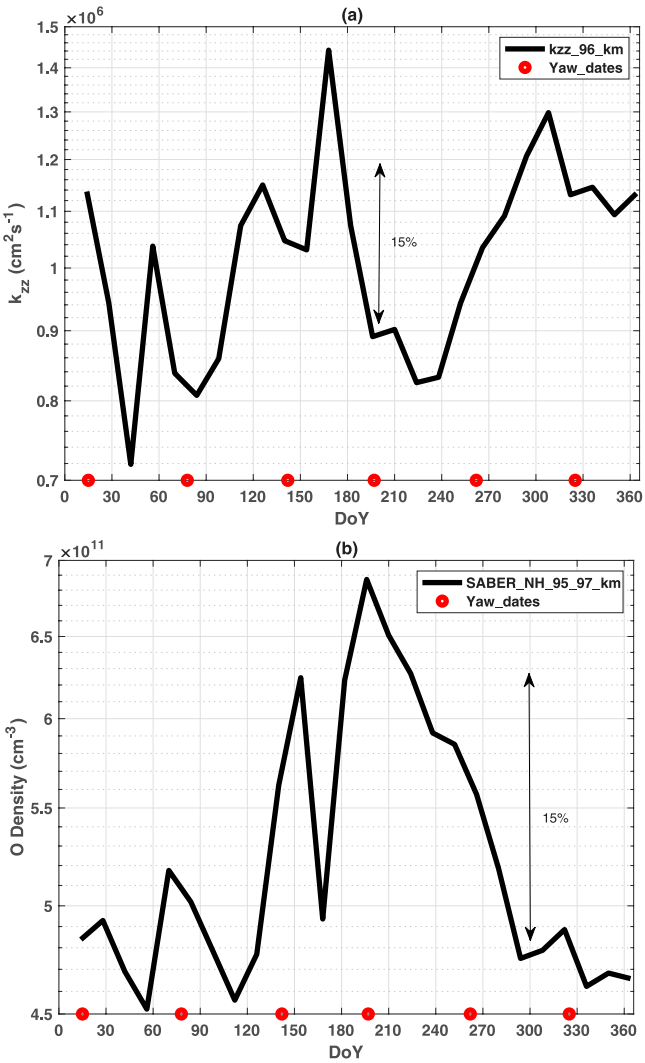

Figure 7. The intra-annual variation of (a) k_{zz} and (b) O density for SABER at 96 km are shown with the vertical double arrow illustrating a fractional amplitude indication. The circles are the days of the satellite yaw events, each year. The relatively large 'spike' at day 170 in k_{zz} in (a) and depletion in O density (b), is referred to as the P2 event.

of zonal momentum fluxes to have variability in altitude and season similar to the k_{zz} variability described in Figure 3b. This study also demonstrates the significant effect the tidal phases have on diurnal variability.

We computed the difference in the integral loss of O between 80 and 96 km in winter versus summer due to the AO, using the SABER profiles shown in Figure 6. The calculated difference in O loss between summer and winter solstice due to k_{zz} corresponds to a change of 20% in the downward flux of O at 96 km. That difference should reflect the change in either the diffusion velocity (k_{zz}) or O density or a combination of both. The change was 20%, from the winter minimum to the summer maximum, or an oscillation amplitude of 10%. We note there is no change in the global average k_{zz} at the solstice (Figure 6b). According to the observational evidence from SABER and SCIAMACHY, the IAV in the diffusion velocity at 96 km is minimal throughout the annual cycle. The evidence lies in the variation in the O density, and an initial study by Smith et al. (2010). A study of O variation with season was accomplished by Chen et al. (2019), who measured O density oscillations using the GOMOS instrument, and analyzed the AO, SAO, and QBO amplitudes for a few years of observations. These observations complemented studies by Zhu et al. (2015), Lednyts'kyy et al. (2017), and followed by Chen et al. (2019) where amplitudes of the AO were 11%, 7%, and 9.6%, and for the SAO 15%, 12%, and 18%, respectively. The study performed by Chen et al. (2019) had three zones: 20–30°N, −20 to −30°S and an equatorial band. The intra-annual variation of the O density for SABER NH, SH, and EQ versus day number is shown in Figure 7a, and for both SABER and SCIAMACHY in the NH in Figure 7b. Clearly, the amplitudes of the AO for atomic oxygen are consistent with the climatologically determined loss of O in the MLT.

The IAVs in k_{zz} at equatorial latitudes exhibit a more prominent SAO (Figure 9), with larger amplitude at the spring equinox (2X) with respect to a summer minimum than the fall (1.5X). The SAO amplitude is reduced below 85 km. The EQ region ±15° is dominated by the influence of the Inter-Tropical Convergence Zone (ITCZ) in the lower atmosphere, a key factor in forcing the diurnal tides. These results are consistent with the theory described by Dunkerton (1982), which hypothesized that an observed SAO variability in the zonal wind at equatorial latitudes (Hirota, 1978) combined with Kelvin waves selectively enabled gravity waves to propagate into the mesosphere. The enhanced values of k_{zz} that extend well into the upper mesosphere are consistent with this hypothesis. IAV observations of meteor radar winds at Jicamarca (∼12° N, Guo & Lehmacher [2009]), illustrate strong tidal oscillations, with the largest amplitudes at spring and fall equinox, nearly identical to the equatorial IAV amplitudes of k_{zz} derived herein. This result strongly supports the consideration that wave-tide coupling is directly responsible for the larger k_{zz} amplitudes at the EQ versus NH and SH, in the 80–90 km altitude region (Li et al., 2005). illustrates a form of wave-tide coupling interaction with the diurnal tide observations at low latitudes, where Mesospheric Inversion Layers associated with vertical mixing and turbulence, form with a tidal phase. In addition, a secondary consideration involves the Quasi-Biannual Oscillation (QBO). Swenson et al. (2018) described a QBO variation in k_{zz} at EQ latitudes, also with reduced amplitude at 83 km compared to higher altitudes, likely due to the wave filtering by the QBO at lower altitudes.

The AO in k_{zz} affects altitudes below 87 km (Figures 3b, 3f, and 5b), whereas the SAO extends to 96 km, the upper limit of SABER (Figure 3d and 9a–9c). The near constant k_{zz} versus altitude for the SAO enhanced equinox regions is clearly shown in Figures 4 and 5. A possible explanation for the extended altitude region of the SAO is wave-tide coupling. The large amplitude in the diurnal tide (DT) at equatorial latitudes results in a wave-tide interaction (e.g., Li et al., 2005). Figure 10a depicts the k_{zz} profiles for both the annual average for the NH and

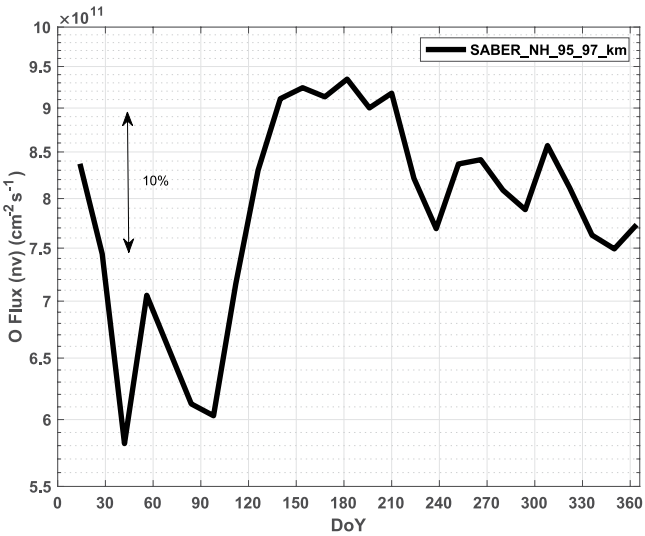

Figure 8. The intra-annual variation of the SABER eddy flux in the northern hemisphere at 96 km. The flux has a maximum in summer, with lower values in fall, and significantly lower in spring. The vertical arrow illustrates the required change between summer and winter solstice necessary to account for the change in the loss of O (and increase in k_{zz}) below 87 km, shown for SABER in Figure 6.

SH, representing the mid-latitude and the EQ. The fact that the EQ profile is uniform with altitude, not just at equinox periods but throughout the year, supports the hypothesis that the wave-tide coupling influences the vertical distribution of turbulence in the EQ region. The fact that the average k_{zz} is 2–3X larger for the EQ than for the NH/SH is consistent with the ITCZ being a strong convective source of gravity waves. The upward propagating waves experience minimal stratospheric filtering at the equator. Wave coupling with the large amplitude diurnal tide results in a significantly larger eddy diffusion effect in the EQ MLT.

Historically, k_{zz} (and the diffusion velocity) have been used as a parameter to drive composition effects in a number of general circulation models. Colegrove et al. (1965, 1966) used this approach to define the k_{zz} relationship to the bi-directional flux (*nv*) of atomic and molecular oxygen. S18 modified the original approach and solved for the diffusion velocity only. We understand today that atomic oxygen can be influenced by a host of other considerations including production, loss, and transport by waves, on the scales discussed herein. In a given hemisphere, the summer produces more O via photodissociation than in the winter, whereas the meteorology and forces from below that are responsible for the eddy velocity and downward transport to O loss do not necessarily map to the production timeline. The intra-annual diffusive coupling between 140 and 96 km is primarily due to molecular diffusion throughout the altitude region, as well as eddy diffusion below ∼105 km. Diffusion upward into the thermosphere reflects the AO that is well documented in the very early thermospheric composition models, for example, Jacchia (1964) where thermal expansion in the thermosphere is important, where O densities vary diurnally by 100%. On the contrary, a 20% change in atomic oxygen density which is the maximum change between the AO solstice extremes, imparts a relatively minimal change to the thermosphere. The k_{zz} deduced by (Qian et al., 2009), which was derived from thermospheric observations, includes SAO and AO amplitudes where the AO (January and July) amplitude is as large as the SAO amplitude. The total time for atomic oxygen production to the altitude of O(^{1}S) emission was observed by Lednyts'kyy et al. (2017) using the correlation between the emission and solar rotation. The chemical loss of O primarily occurs below 93 km, with a peak loss near 87 km. The O density above 93 km is a reservoir of O that is diffusively and dynamically coupled, wherein there is time variation in that coupling that is dependent on the values of the k_{zz} and the spectrum of upward propagating large-scale waves of lower atmospheric origin that dissipate in that region. It is the eddy diffusive process and thus k_{zz} in models, largely below 93 km, that supports the chemistry of O loss.

Derived k_{zz} at 96 km is compared to Qian et al. (2009) in Figure 13. The global average k_{zz} from this study of MLT composition effects retains the EQ zone dominant SAO. The "top-down" approach of (Qian et al., 2009) yields a much larger k_{zz} amplitude, that is out of phase with the dynamical-chemical balance approach employed herein. The message here is the climatology of the O density and k_{zz} dominate the vertical transport, and the global mean has little value to a model that is describing the composition since seasonal effects dominate. In particular, the O density and k_{zz} with the NH versus the SH are dramatically different for a given time, and when analyzing satellite data for a given orbit, the respective hemispherical responses should be kept separate, in order to account for the dominant seasonal influences.

5.1. Implications for the Overlying Thermosphere and Ionosphere IAVs

The IAVs in k_{zz} that we have deduced will naturally have implications for upper thermospheric and ionospheric IAVs (e.g., Qian et al., 2009, 2013; Yue et al., 2019) through seasonally-dependent transport of atomic oxygen in the MLT region (Jones et al., 2017, 2018). The k_{zz} analysis by Qian et al. (2009) include both the AO and SAO components, with the AO amplitude at a solstice similar to the SAO amplitude. Figure 13 clearly shows an SAO in global average k_{zz} that is consistent with CO_2-derived k_{zz} results from (Salinas et al., 2016), and is much weaker than what Qian et al. (2009) inferred from satellite drag data in the upper thermosphere. Taken with the Salinas et al. (2016), our weaker IAVs in k_{zz} indicate that the overlying thermosphere and ionosphere SAO is not primarily

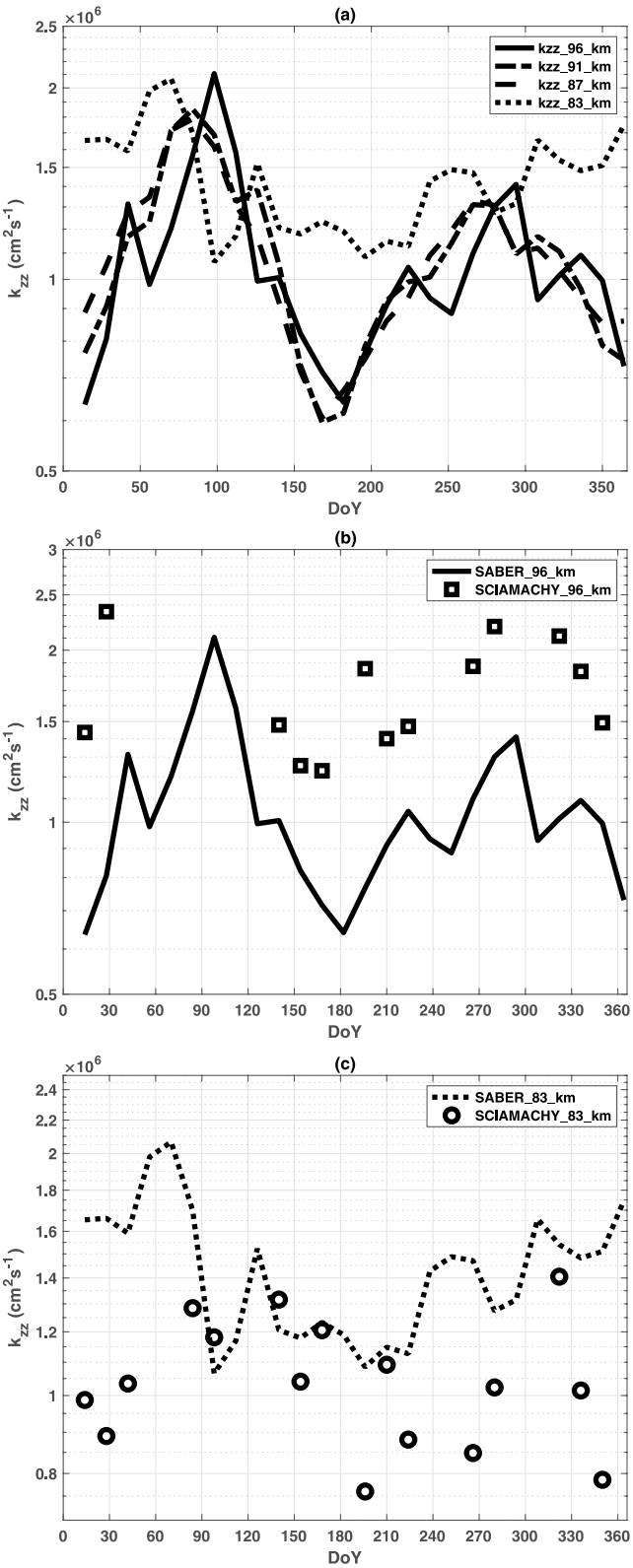

Figure 9. (a) k_{zz} versus DoY for EQ 96, 91, 87, and 83 km for SABER. The spring equinox is the dominant oscillation at all altitudes. (b) Same as (a) except at 96 km for SABER and SCIAMACHY, and (c), same as (b) except for 83 km.

driven by IAVs in k_{zz}, but rather acts in concert with the predominant thermospheric spoon mechanism (Fuller-Rowell, 1998; Jones et al., 2018).

Further, our k_{zz} deduced from SABER O, is of opposite phase relative to those either produced by gravity wave drag parameterizations or invoked in the NCAR thermospheric general circulation models (see Jones et al., 2017; Qian et al., 2009). This oppositely-phased IAV in k_{zz} calculated herein is likely due to IAVs in the SABER O density (see Smith et al., 2010), and thus deduced downward O fluxes calculated for in the MLT region. Differences between IAVs in k_{zz} deduced from SABER O using Equations 1–4 and, for example, the NCAR thermosphere-ionosphere-mesosphere-electrodynamics general circulation model is probably because the atomic oxygen flux in Equations 1 and 2 are the total vertical flux of atomic oxygen, including eddy and molecular diffusion and the "bulk" vertical wind (see Jones et al., 2018, 2021). While upper thermospheric general circulation models are able to separate all these different processes, assumptions made in Equations 1–4 lead to a slight convolution between the eddy diffusive flux and "bulk" vertical wind flux of O.

Potentially, most important for upper thermospheric and ionospheric IAVs are the results presented in Figures 4 and 5, which show a strong AO in k_{zz} at middle northern and southern latitudes. To our knowledge, unless one uses a large AO in k_{zz} (like Qian et al., 2009) in the MLT region, upper atmospheric general circulation models do not accurately reproduce the observed AO in thermospheric mass density and ionosphere electron density. Therefore, the latitudinal dependence of IAVs in k_{zz} within such models should be re-evaluated given our results. Perhaps, one might expect these upper atmospheric general circulation models would produce a more realistic thermospheric and ionospheric AO in pertinent model parameters if they properly accounted for the latitude and seasonal dependence of k_{zz} IAVs deduced from SABER. Such reasoning is further supported by recent results from Malhotra et al. (2020), which quantified the sensitivity of middle-upper thermospheric dynamics, energetics, and composition to changes in O density between the 95–100 km in the global ionosphere thermosphere model (model lower boundary at 95 km).

The temperature profile between 95 km and the thermosphere is an important attribute in the diffusive coupling of composition between atmospheric regions, especially for projecting compositional IAVs into the upper thermosphere and ionosphere (see Jacchia, 1970 and Equations 1 and 4 herein). Temperature measurements from SABER CO_2, as well as Gobal-scale Observations of the Limb and Disk and Ionospheric CONnection Explorer satellite measurements, will provide improved temperature IAVs, for the models above to validate against. The modeling studies above clearly demonstrate that eddy diffusion, neutral wind transport, and temperature all play an important role in MLT coupling of composition with the thermosphere. Further, seasonal production and loss also play a role for O. With these new space-based assets, providing long-term datasets, we are starting to be able to truly assess the ability of our general circulation models in the middle and upper atmosphere."

5.2. Effects and Uncertainties Due to Advection

Contamination of the vertical gradient and density of O in a zone can occur as a result of meridional advection from one zone to another, and by vertical advection within a zone. The midlatitude zones (NH, SH), between 80 and

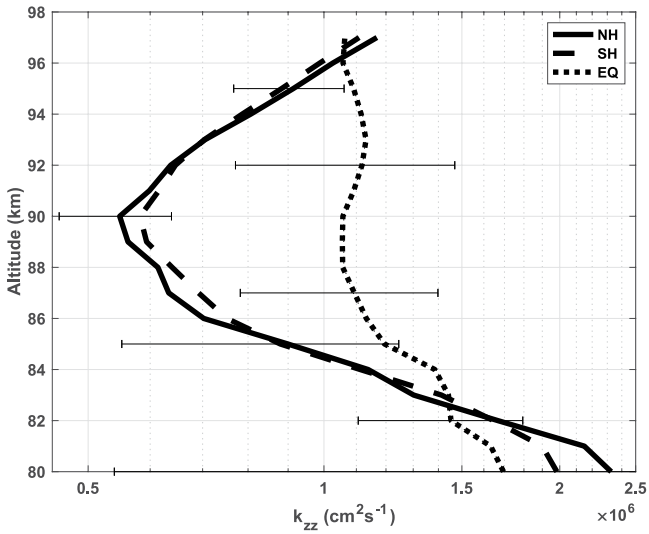

Figure 10. Annual average k_{zz} versus altitude values for SABER, for the northern hemisphere (NH), southern hemisphere (SH), and equatorial (EQ) zones. The NH and SH profiles are nearly identical. Note the EQ profile is almost constant with altitude. The horizontal bars indicate the standard deviation at 92, 87, and 82 km for the EQ and at 95, 90, and 85 for the NH for the 16 years of SABER measurements.

90 km are the zones where there is a strong seasonal difference in k_{zz} (and diffusion velocity) that are subject to contamination of the O densities by either (or both) vertical and horizontal advection. The AO, driven by the residual circulation below 90 km, is a condition of significant duration (weeks), that has a significant amplitude in both meridional and vertical winds. Analysis for determining these effects on the eddy diffusion coefficients calculated herein involved a close examination of the altitude distributions of the diffusion velocities and time to reach an equilibrium state, the chemical lifetime relevant to advected O from one zone to another, and the climatology of meridional advection velocities associated with contamination from adjacent zones. A detailed analysis is provided in Appendix D supporting the summary given below.

Our findings for the mid-latitude, AO amplitude of the vertical upwelling at summer solstice was estimated to be 0.4 cms^{-1} at 80 km. The chemical lifetime at this altitude is ∼1 hr, resulting in penetration of 15 m at that altitude (see Appendix D3), a negligible uncertainty to the vertical distribution of O density and k_{zz} calculations herein. Similarly, horizontal advection at 85 km, was calculated given a 3 ms^{-1} horizontal advection velocity at the boundary between the NH and the EQ, with a zone penetration of 10 hr (the chemical lifetime, see Appendix D4). The rationale is that advected O traveling further into the zone would recombine, and its vertical distribution due to diffusion would dominate over advection. The calculated penetration is ∼1° in latitude, contaminating 1/30th (or 3.3%) of the EQ zone. The penetration volume is assumed to be 50% contaminated with respect to chemical loss of O, for uncertainty due to horizontal advection of 1.7%. These relatively small uncertainties allow the latitude zones to be made smaller below 90 km, in future studies.

Above 88–90 km, the diffusion times are less than the chemical recombination time. At 96 km, for example, a 4-day penetration of 3 ms^{-1} results in a 10° invasion of the EQ zone resulting in a 33% area contamination, and at 50% contamination, results in a 16.5% uncertainty. In the lower thermosphere the effects and uncertainty due to vertical advection are complicated due to the various circulation patterns at these altitudes, for example, by the mesospheric residual circulation (e.g., Garcia & Solomon, 1985), or the lower thermospheric residual circulation at 95–110 km (e.g., Qian and Yue (2017), or both, depending on the season, altitude, and latitude. Further, Jones et al. (2018) demonstrated that the thermospheric spoon mechanism is most effective in the altitude regime where the thermosphere is transitioning from a fully mixed state to a diffusively separated state, indicating that the vertical advection/transport effects may also contribute to this uncertainty. Finally, as acknowledged above, the total vertical flux of atomic oxygen calculated for in Equations 1 and 2, is really the aggregate effect of the eddy, molecular, and "bulk" vertical wind on O, and thereby ultimately driving uncertainty in k_{zz}.

However, modeling studies suggest that the coupling from above the MLT region is mainly due to molecular diffusion (see Figure 4b in Jones et al., 2017). For example, summing O densities above 140 km versus the columnar O density between 90 and 140 km leads to a ratio of ∼0.075 (or 7.5%). If we then assume, for example, a ∼30% change in O densities due to redistribution of O in the thermosphere, given diffusive equilibrium (dominated by molecular diffusion above 115 km), there would be less than a ∼2.3% change in the 90–140 km O density. That small change would have minimal effects on the determination of k_{zz}.

In summary, the advection contamination at lower altitudes (below 90 km) where O lifetimes associated with recombination are short, vertical and horizontal advection contamination is minimal. At higher altitudes 90–96 km, advection can lead to uncertainties that approach 10%–20%, at the EQ. Given the discussion in the previous paragraph, uncertainties due to advection in the thermosphere would best be accomplished by refined global circulation models which would incorporate the details of the vertical distributions of temperature, composition, and dynamics. The contrast in the results between the EQ and NH/SH, where the strong SAO in the EQ zone and nearly absent in the NH, strongly suggest that even between 90-96 km, contamination from horizontal advection effects between those two zones is minimal.

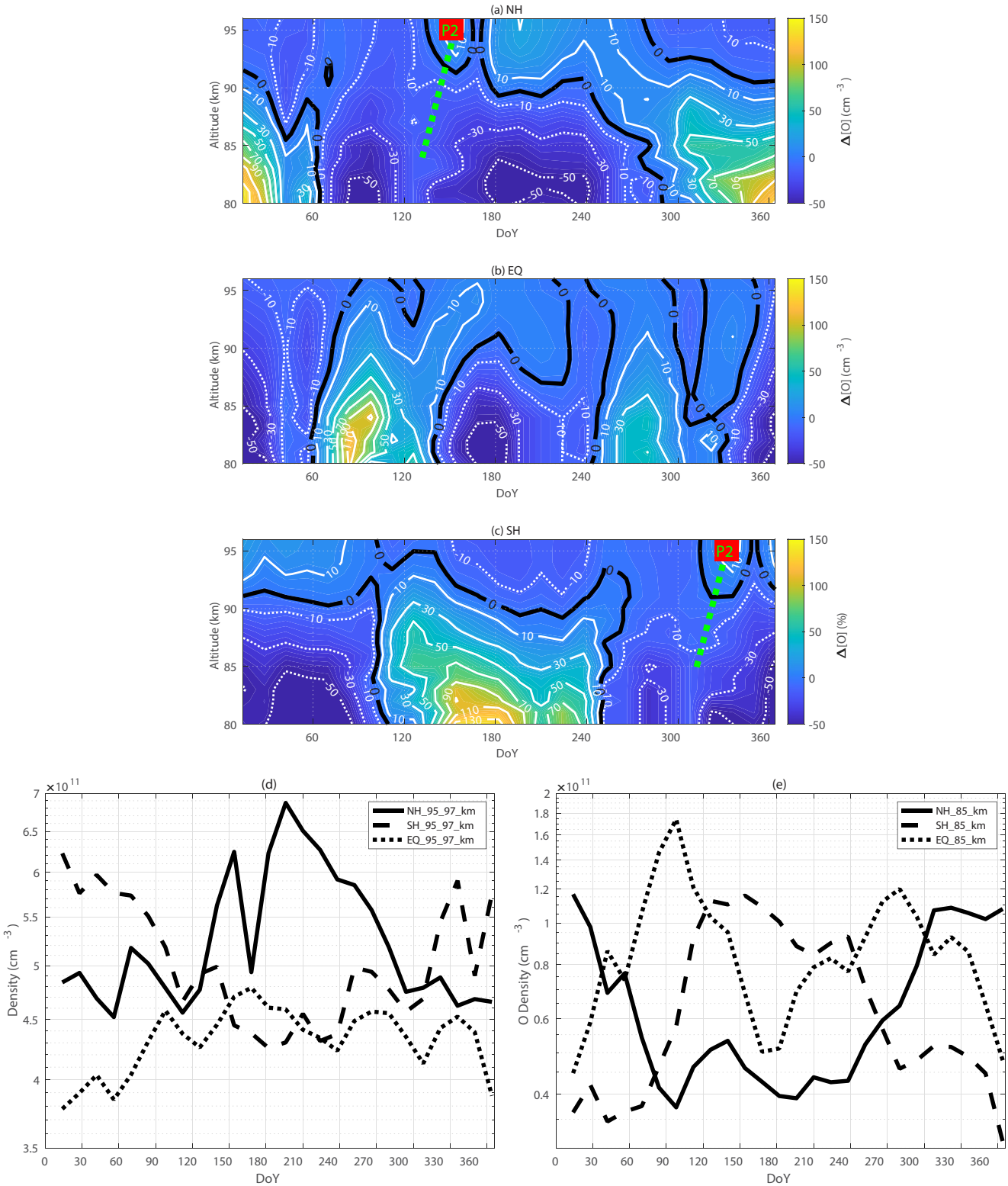
(a) NH
(b) EQ
(c) SH
P2
Altitude (km)
DoY
Δ[O] (cm -3)
Δ[O] (%)
(d)
(e)
Density (cm -3)
O Density (cm -3)
NH_95_97_km
SH_95_97_km
EQ_95_97_km
NH_85_km
SH_85_km
EQ_85_km

Figure 11.

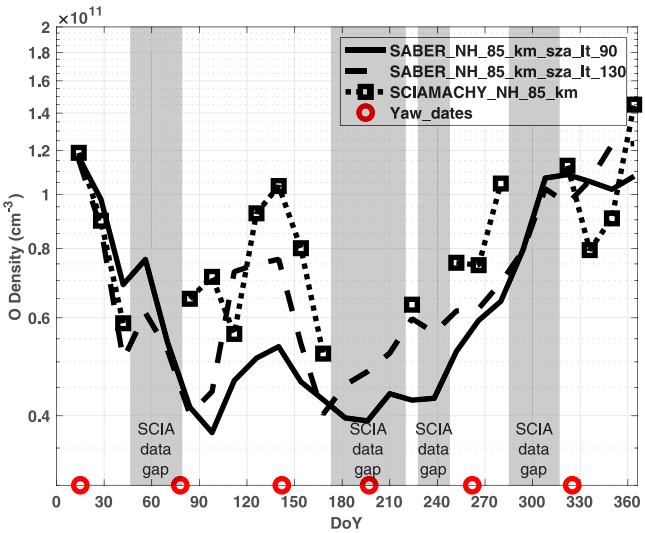

Figure 12. Northern hemisphere O density versus DoY, at 85 km. The SABER nighttime data (solid line), SABER SZA> 130° (dashed), and SCIAMACHY data (squares) are shown. Both SABER and SCIAMACHY clearly identify the P2 brightness enhancement. The amplitude effects of the P2 event include local time sampling biases, which are discussed in the text. Note the SCIAMACHY data gaps and SABER Yaw dates are indicated.

5.3. Additional Uncertainties and Future Studies

Figure 14 shows the near global (±55° average of k_{zz} altitude profiles for SABER. The main difference between this study and S19) is an increase in the total profile by a factor of ~2 at 83 km to 1.5 at 96 km. The primary reason for this is a lesser amount of O in the mean O profiles which leads to an increased k_{zz} in order to meet the flux integral (Equation 2) from the 80 km lower boundary condition. Additional minor contributions are attributed to (a) the method of averaging k_{zz} from the three zones, for the 26 periods in the annual cycle, rather than computing a global mean from the global mean O density profile, (b) MSIS2.0 that contains the relevant background atmosphere affecting the chemistry of O loss for each of the 78 temporal/spatial conditions, and (c) the O density was determined for nighttime conditions only, whereas the earlier study determined O density for day and night conditions. The O density uncertainties increase to a lower limit of 80 km, contributing to the uncertainty in k_{zz} below 83 km (Figure 14). The chemical model was described by Mlynczak et al. (2013, 2018). Table 2 in Mlynczak et al. (2018) describes uncertainty of 20%, whereas the analysis by Mast et al. (2013) describes a smaller error. The uncertainty in k_{zz} is less sensitive to O density but strongly sensitive to the gradient. A case study changing O density by 20% uniformly in altitude above 80 km resulted in a change in k_{zz} of 1.6% at 96 km, increasing with decreasing altitude to 2.0% at 89 km, 3.0% at 84 km, and 6.3% at 80 km. The statistical uncertainties of 16 years of limb data inversions with geophysical variations of waves (gravity waves, tides, and planetary) contributions are unknown, but we believe less than those due to the uncertainties in the O density.

Clearly, the sophisticated approaches to define, track, filter, and propagate the meteorological effects from below as was done by Becker and von Savigny (2010); Grygalashvyly et al. (2012); A. Z. Liu et al. (2016), among others are evolving and constantly being improved. As the coupling of the atmosphere from the troposphere to the thermosphere is developed, the climatology of the minor constituents in the MLT, and parameterized transport effect from these climatologically driven studies, will play a role in refining and improving the process, with model validation.

6. Conclusions

The intra-annual variation of eddy diffusion in the MLT region has been quantified using an analysis of the observed, average atomic oxygen profiles at 80–96 km by the TIMED-SABER instrument (2002–2018) and 80–105 km by the Envisat SCIAMACHY instrument (2002–2014). The analysis method described for the determination of global mean k_{zz} by S19 was used, along with the background atmospheric species were determined by the MSIS2.0 model (Emmert et al., 2021).

A list of our prominent findings are as follows:

1. The AO variation in k_{zz} peaks in summer (near solstice) and is at a minimum in winter, with an amplitude factor change of ~4X between solstices, in both the NH and SH at 83 km.
2. The difference between the winter and summer losses of O require an AO amplitude in the downward flux (nv) at 96 km, for 10%. The intra-annual variation of the eddy diffusion velocity (v) is invariant at that altitude, but the O density is not, with measurements and analysis by Chen et al. (2019). The minimal O density below

Figure 11. The intra-annual variations (IAV) of the percentage change in O density versus altitude, relative to the zonal mean altitude profile for the northern hemisphere (NH) (a), equatorial (EQ) (b), and southern hemisphere (SH) (c). (d) The IAV in SABER O density at 96 km and (e) for 85 km. Note the AO amplitude phase switches from a summer maximum at 96 km, to a winter maximum at 85 km, where the minimal O density coincides with the maximum in k_{zz} at low altitude (see Figures 3, 4, and 5b). Also note the significant EQ spring equinox amplitude at 85 km, in phase with the magnitude and vertical extend of k_{zz} (Figures 9a–9c), rather than out-of-phase. Note event P2 with a maximum near the upper altitude of the sampling altitudes at 96 km near DoY 170 in the NH (a) and ~180 days later in the SH, (c).

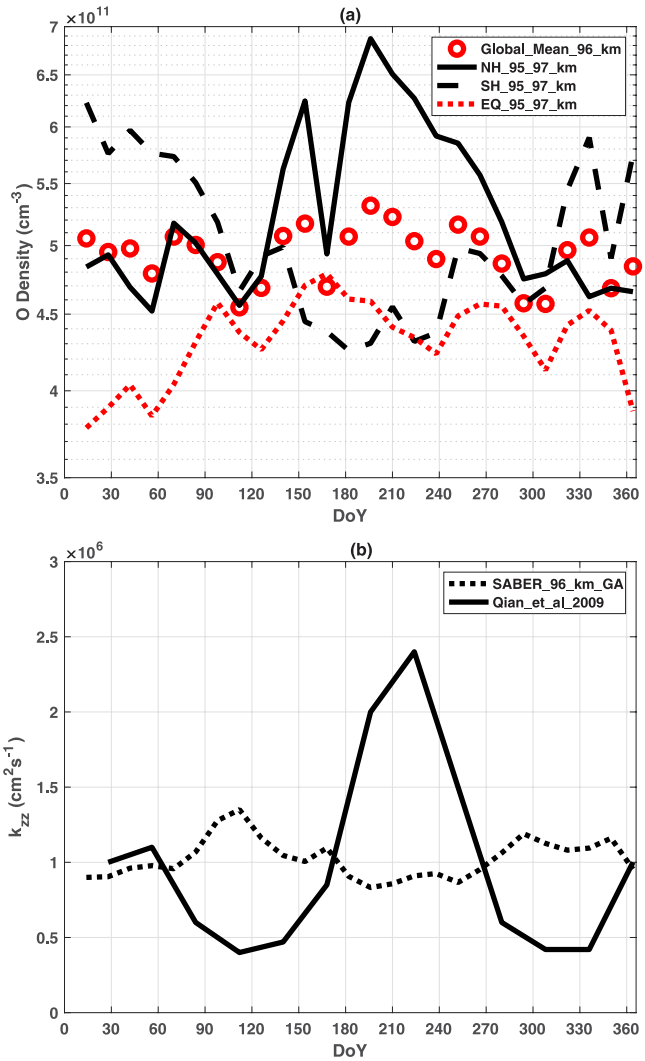

Figure 13. The global average of O density (a) versus day of year for SABER at 96 km (Solid circles). The northern hemisphere, southern hemisphere, and equinox are also plotted for perspective. There is a negligible difference between winter and summer, although the SAO is clearly dominant. (b) The global average k_{zz} versus day of year for SABER at 96 km (dotted) and Qian et al. (2009) (solid). The mean k_{zz} for the two plots is nearly identical, but there are significant differences in the intra-annual variations.

90 km in the mid-latitude summer is consistent with enhanced depletion and chemical O loss in summer.

3. The analysis of k_{zz} in the EQ region resulted in a large SAO amplitude of 25% from solstice to spring equinox, and less from solstice to fall equinox.
4. The EQ k_{zz} annual-average profiles are uniform with altitude, with a value of 1.1×10^6 cm^{2}s^{-1}. The vertical extent of the large k_{zz}, the upper limit of the data at 96 km, likely contributes to the simultaneous increase in O density, rather than the opposite effect, observed at mid-latitude with the AO cycle. The uniformity with altitude and significantly larger SAO amplitude support the hypothesis that wave-tide coupling contributes to turbulence and wave mixing at all EQ altitudes. The stratospheric wind minimum at the EQ also likely minimizes the filtering of waves reaching the MLT.
5. The climatology of the MLT k_{zz} supports the Qian et al. (2009) annual mean, but not the intra-annual variability in the downward flux at 97 km, similar to what was reported by Salinas et al. (2016). The variation in the AO (at solstice) is partially due to the variability in the O density, and consequently, the downward flux, which is highly variable with season. The intra-annual global mean k_{zz} and O density in global models would be best replaced with seasonal effects for the respective hemisphere, in order to better represent coupling effects taking place in the MLT.

Appendix A: Definitions

The terms for Equations 2–4 are defined as:
D_{ij}: mutual diffusion coefficient for ith and jth gases;
($D_{O,N_2} = 0.26(T/T_0)^{1.76}(P_0/P)$)
D_i: species molecular diffusion coefficient; ($1/D_i = \sum_{j \neq i} n_j / N D_{ij}$);
g: acceleration of gravity;
H: scale height ($\kappa T/mg$);
H_i: species scale height ($\kappa T/m_i g$);
k_{zz}: eddy diffusion coefficient;
κ: Boltzmann constant;
m_i: species molecular weight;
m: mean molecular weight;
n_i: density of ith constituent;
N: total density ($N = \sum_i n_i$);
ϕ_i: species flux ($\phi_i = n_i v_i$);
T: temperature;
v_i: species diffusion velocity for ith species;
z: geometric altitude.

Appendix B: Equation 2 Chemistry

The chemistry describing the first term in Equation 2 is described in the text. The second and third terms were described in S18 and are repeated here for completeness.

The second consideration of O loss is the three-body recombination, that is,

$$O + O + M \xrightarrow{k_4} O_2 + M \tag{B1}$$

for $k_4 = 2.7 \times 10^{-33}$, where 2 atomic oxygen atoms are lost; and consequently,

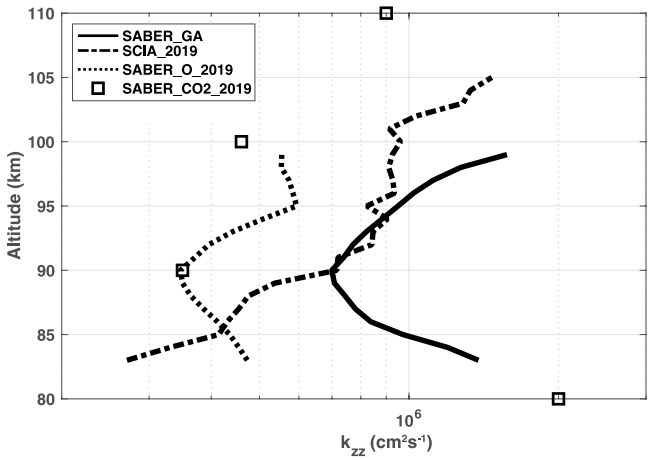

Figure 14. k_{zz} versus altitude for the global average (GA) SABER O from this study compared with the SABER O and CO_2 and SCIAMACHY O derived results in S19.

$$L(3body) = -2k_4[O][O][M] \quad \text{(B2)}$$

The chemistry for the third term in Equation 2 is the loss due to HO_2 is also a consideration, that is,

$$H + O_2 + M \xrightarrow{k_6} HO_2 + M \quad \text{(B3)}$$

where $k_6 = 4.4 \times 10^{-32}(300/T)^{1.3}$, and subsequently forms an OH, where one O is lost, that is,

$$O + HO_2 \xrightarrow{k_7} OH + O_2 \quad \text{(B4)}$$

for $k_7 = 3.0 \times 10^{-11}$ exp(200/T).

Appendix C: k_{zz} Values for Figures 3b–3f

Figures C1, C2, and C3 below contain the values of k_{zz} for the NH, EQ, and SH zones shown in Figures 3b–3f, respectively, in units of m^2s^{-1}.

IAV #		1	2	3	4	5	6	7	8	9	10	11	12	13	14	15	16	17	18	19	20	21	22	23	24	25	26
	Alt (km)																										
NH																											
	80	56	63	67	70	107	152	216	187	262	323	392	452	634	583	474	435	411	329	223	155	109	82	71	67	66	64
	81	72	70	82	92	119	164	170	191	218	239	323	417	585	527	475	416	334	247	192	149	124	93	75	71	73	71
	82	70	76	92	91	97	111	141	169	170	182	246	323	404	366	324	273	230	163	125	105	112	104	101	95	86	80
	83	72	74	82	65	72	87	121	133	152	180	221	259	261	262	233	211	173	129	98	90	72	58	66	70	72	71
	84	67	64	74	68	67	87	101	111	134	176	211	210	190	208	182	173	150	115	104	102	71	50	56	59	66	65
	85	64	64	70	61	56	57	65	79	91	123	152	158	142	149	138	132	113	81	71	66	67	62	70	73	68	67
	86	65	61	59	49	41	43	52	63	76	99	112	123	104	109	103	96	78	62	52	49	49	46	54	57	61	61
	87	61	56	58	51	39	44	56	69	78	94	90	95	81	81	78	74	63	57	55	55	49	46	50	52	57	59
	88	65	59	58	55	40	42	49	63	73	90	79	79	63	66	66	64	59	55	56	55	54	58	60	61	61	65
	89	69	59	49	53	37	35	39	54	63	74	68	73	56	57	58	58	55	51	48	46	53	63	60	60	61	63
	90	67	57	47	58	37	35	40	56	64	65	59	68	52	50	53	51	49	48	50	52	57	66	62	61	60	64
	91	78	64	51	64	45	42	45	62	72	63	54	67	53	48	53	51	49	53	57	60	65	77	73	71	67	73
	92	82	69	53	68	51	47	47	64	73	65	55	69	58	49	54	51	52	57	62	66	72	89	78	78	73	76
	93	87	72	54	75	59	54	54	71	81	68	60	82	64	55	62	56	57	63	69	74	85	95	88	86	79	83
	94	98	79	61	82	66	64	65	82	92	77	72	96	79	65	69	64	64	74	78	86	99	106	96	97	91	92
	95	105	89	68	92	77	75	74	95	102	93	83	120	91	74	83	71	72	83	91	97	109	118	107	105	100	102
	96	114	94	72	104	84	81	86	107	115	105	103	144	107	89	90	82	83	94	103	109	121	130	113	115	109	113

Figure C1. k_{zz} versus altitude for the northern hemisphere.

IAV #		1	2	3	4	5	6	7	8	9	10	11	12	13	14	15	16	17	18	19	20	21	22	23	24	25	26
	Alt (km)																										
EQ																											
	80	183	170	180	184	140	129	106	134	137	164	217	246	251	202	175	172	186	166	143	132	150	154	153	158	186	190
	81	209	177	139	160	142	131	137	160	144	141	168	215	221	193	188	197	179	152	145	148	153	157	126	131	148	183
	82	266	199	141	175	174	136	109	125	134	111	122	144	140	126	124	130	138	144	131	122	127	151	136	125	142	207
	83	165	166	159	198	207	170	107	117	152	121	118	123	119	108	115	113	143	149	147	127	132	166	154	148	151	175
	84	130	131	146	153	209	202	145	135	147	125	115	125	118	108	114	123	145	153	165	157	135	140	124	114	119	124
	85	119	131	141	141	184	191	151	115	122	96	88	93	83	88	97	107	115	139	147	132	112	113	105	95	95	105
	86	106	113	134	148	176	184	161	125	113	91	72	68	68	78	89	96	107	123	135	127	126	115	106	95	89	100
	87	89	105	127	135	172	179	162	131	116	92	72	61	67	75	86	94	109	119	133	131	110	112	103	94	85	86
	88	84	99	125	142	159	174	162	120	119	93	69	58	62	75	83	91	102	117	128	124	108	109	101	87	79	77
	89	79	94	122	140	153	164	166	142	117	92	68	54	60	73	84	91	106	117	125	124	121	113	98	89	76	76
	90	75	95	117	122	157	168	164	142	123	95	69	54	61	75	88	95	105	115	129	129	115	112	102	90	77	73
	91	77	91	117	123	171	185	169	133	138	106	73	60	62	79	93	99	101	114	131	131	110	117	111	97	79	75
	92	75	90	122	117	169	204	181	136	136	115	78	58	63	81	97	100	99	112	131	133	118	114	111	106	85	78
	93	72	89	128	104	163	212	197	141	132	121	84	62	66	85	102	104	97	106	129	140	120	102	114	108	88	76
	94	72	85	127	95	152	211	215	136	119	119	83	65	67	87	101	107	92	96	119	137	123	98	113	111	92	77
	95	70	85	127	95	138	187	222	145	109	112	89	69	65	80	97	106	92	90	109	130	137	93	104	111	98	76
	96	64	81	131	98	120	157	211	158	99	101	82	72	64	77	91	105	94	88	110	130	141	93	101	109	100	73

Figure C2. k_{zz} versus altitude for the equator.

IAV #		1	2	3	4	5	6	7	8	9	10	11	12	13	14	15	16	17	18	19	20	21	22	23	24	25	26
	Alt (km)																										
SH																											
	80	413	355	426	388	339	208	137	98	84	85	77	66	62	59	60	62	70	86	107	171	155	208	287	325	314	515
	81	434	359	390	372	288	190	131	101	76	66	65	70	73	78	80	75	68	81	135	160	170	196	205	252	321	501
	82	396	348	328	266	212	152	117	107	99	73	68	70	72	73	66	72	77	99	115	107	147	148	165	218	292	393
	83	313	266	258	204	175	128	112	74	69	83	88	79	74	74	67	75	73	71	67	88	117	135	174	221	261	324
	84	225	195	187	155	128	122	116	68	47	54	62	65	68	67	64	66	57	49	61	89	101	116	140	161	191	238
	85	158	156	129	105	91	95	97	70	54	53	60	63	62	57	54	62	57	53	67	60	70	79	97	118	155	165
	86	130	122	97	81	71	66	71	56	55	63	71	67	64	59	53	65	57	53	43	45	59	69	84	103	135	117
	87	104	102	86	76	64	60	69	58	47	53	65	63	63	60	56	58	52	38	37	47	64	74	91	101	118	94
	88	84	85	73	66	55	61	71	67	54	53	62	61	60	56	50	55	55	38	42	48	57	70	77	87	98	79
	89	70	76	61	54	46	48	51	64	64	62	70	66	65	55	50	61	58	44	39	40	49	59	66	72	86	68
	90	62	69	54	51	46	43	46	66	70	68	76	69	68	61	54	60	59	42	38	40	52	62	62	65	76	58
	91	59	68	55	54	49	47	51	75	79	71	79	74	71	63	58	60	64	46	44	46	58	70	65	63	75	57
	92	58	69	56	55	49	53	50	81	91	79	87	77	73	65	59	65	71	52	48	50	60	72	65	64	75	57
	93	63	74	60	59	55	56	56	91	98	88	96	85	79	70	63	68	77	56	54	57	67	77	71	68	79	62
	94	72	78	67	67	66	65	66	105	109	95	103	93	86	73	65	74	83	64	62	67	78	88	80	74	89	75
	95	80	89	76	78	70	73	78	122	121	101	111	102	92	76	72	83	93	70	68	73	85	104	94	92	110	85
	96	93	96	85	91	83	83	87	139	134	108	116	113	101	84	76	86	101	77	72	79	95	115	110	105	139	100

Figure C3. k_{zz} versus altitude for the southern hemisphere.

Appendix D: Advection and Associated Uncertainties in k_{zz}

Contamination of the vertical gradient and density of O in a zone (e.g., NH, EQ, SH) can occur as a result of meridional advection from one zone to another, and by vertical advection within an individual latitudinal zone. The midlatitude zones (NH, SH), between 80 and 90 km are the zones where there is a strong seasonal difference in k_{zz} (and the diffusion velocity) that are subject to contamination of O profiles by either (or both) vertical and horizontal advection. The AO, driven by the residual circulation, is a condition of significant duration (weeks), has a significant amplitude in both meridional and vertical winds.

The vertical advection velocity will be directly compared with the diffusion velocity, in order to establish the fraction of contaminant O. Horizontal advection translates O across a zonal boundary until the time transpired is equal to the diffusion time, or the chemical lifetime of the advected O, whichever is least. The relevant information is organized below: (a) the diffusion velocities, diffusion times, and chemical lifetimes (b) the climatologies of meridional advection velocities, c) the determination of the NH/SH zones by vertical advection, (d) same as (c) except horizontal (meridional) advection. (Note that in our analysis, we are averaging all longitudes, which mitigates zonal advection effects. Also, note the directional convention of the O diffusion velocity is always downward, and in this study as well as S18 and S19, downward is positive.)

Appendix D1: O Diffusion Velocities (Times) and Chemical Lifetimes

The average diffusion velocity at 96 km has been calculated by S18 and S19 studies to be 1.5 cm s^{-1}. This corresponds to a linear translation of O, an estimated distance of ~1.3 km per day at this altitude. The 'diffusion time', to diffuse O from a dissociation source above 110 km to a change in density at 96 km, the altitude of greenline (e.g., O(^{1}S) 557.7 nm emission), was measured by (Lednyts'kyy et al., 2017) to be 14 days. At these altitudes then, the diffusion time of 14 days is a time necessary for MLT atomic oxygen to diffuse to 96 km.

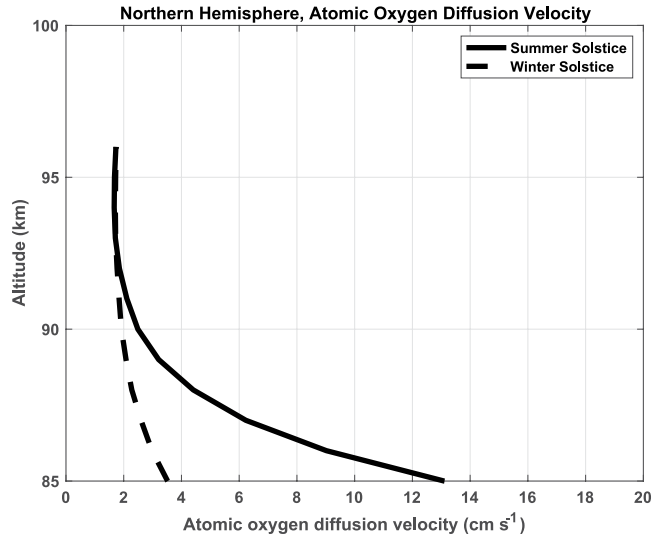

Figure D1. Atomic oxygen diffusion velocity versus. altitude for NH summer and winter solstice (AO) conditions.

The diffusion velocities for the NH at summer/winter solstices are shown in Figure D1. These velocities were determined using Equation 2 with the relevant temporal conditions of SABER O and NRLMSIS 2.0 composition and T for the NH solstice conditions. The diffusion velocity at 96 km is 1.8 cm s^{-1}, but increases at 85 km, the heart of the midlatitude variability, to 3.4 cm s^{-1} (winter) and 13 cm s^{-1} (summer). These diffusion velocities at 85 km to 14 days at 96 km, decreases the diffusion time to 7 days in winter, and to 2 days in summer.

The eddy diffusion velocity in the EQ region (Figure D2) has a minimum near the solstice, and maximum near spring equinox (SAO). These velocities were determined using Equation 2 similar to that for Figure D1 described above, but for the EQ spring equinox conditions. The determination of the diffusion time for the summer at 95 km is 14 days, and at 85 km, 4 days. At spring equinox, the diffusion time at 95 km is 7 days, and at 85 km, 4 days.

Another important consideration is the chemical lifetime or the time it takes a given O parcel to be reduced by a factor of e by the recombination rate in absence of transport. The main loss processes are due to O recombination forming ozone, and as well as the HO_2 chemistry below 85 km (see S18, Figure 4). The expression determining this lifetime follows from Equations 6 and B4, that is:

$$d[O]/dt = (K1 * [O] * [O_2] * [M] + k6 * [H] * [O_2] * [M]) \quad \text{(D1)}$$

Let

$$y(z) = k1 * [O_2] * [M] + k6 * [H] * [O_2] * [M]/[O] \quad \text{(D2)}$$

Then

$$[O] = [O]_o exp\,(y\,(z) * t\,(z)) \quad \text{(D3)}$$

$$y(z) * t(z) = 1; t = 1/y(z) \quad \text{(D4)}$$

Where k1 is defined in Equation 6, k6 is defined in S19, O densities by SABER, and the remaining atmospheric parameter were determined from the NRLMSIS 2.0 model. Above 90 km, 3-body recombination contributes minimally, with a maximum of ~20% at 96 km, the maximum altitude of SABER data (see S18, Figure 4).

The chemical lifetime for the EQ zone is plotted versus altitude in Figure D3. Consider an advection velocity from the boundary of the NH-EQ zones (15° N) for example, The advection process transporting O from an adjacent zone, persists for the distance associated with the chemical lifetime. The advected O is introduced to that distance,

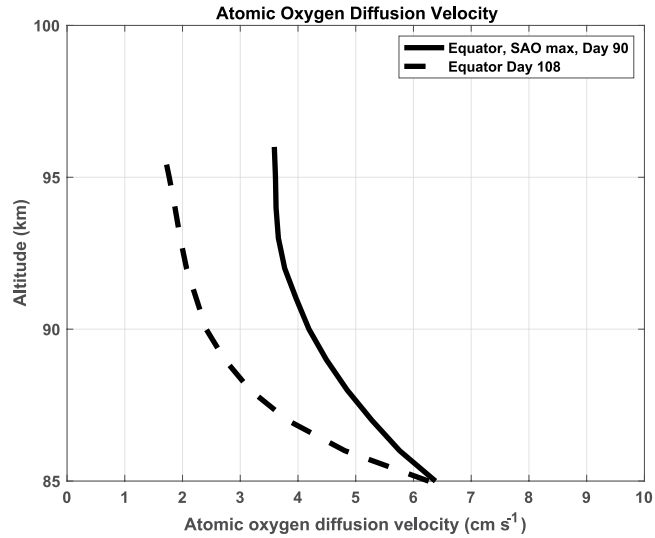

Figure D2. Atomic oxygen diffusion velocity versus altitude for EQ summer and at spring equinox (SAO maximum) conditions.

but beyond that distance, advected O recombines, and vertical diffusion dominates. The chemical lifetime at 85 km, the heart of the variability associated with the AO, is ~10 hr.

At an altitude of 88 and 90 km, the chemical lifetimes are 2 and 5 days, respectively. The chemical lifetime is less than the diffusion times below 88–90 km, and above, diffusion times are greater than the chemical lifetimes. At 96 km for example, the chemical lifetime is ~80 days, a value much greater than the diffusion time (13 days) described by (Lednyts'kyy et al., 2017).

Appendix D2: The Climatologies of Meridional Advection Velocities

The climatological winds between 80 and 96 km have largely been measured by meteor radars, lidars, chemical releases, and rockets. Analysis and modeling of wind data in the MLT have been described in Portnyagin (1986), Vincent (1993), Portnyagin and Solovjeva (1997), and Portnyagin and Solovjova (2000). Figure D4 summarizes meridional advection velocities for relevant latitudes and altitudes. The observations and models of AO meridional winds amplitude of 3–6 ms^{-1} is typical.

Appendix D3: The Determination of Vertical Advection in the NH/SH Zones

The vertical advection velocity transports a lower O density from below 80 km into the MLT where it can be compared with the O eddy diffusion velocity determined in this study. The velocity for the NH summer solstice was computed using conservation of mass. We've chosen to make a calculation due to the residual circulation below 90 km at summer solstice where the upwelling velocity (and flux) has it's largest magnitude. The conservation of mass requires the flux from the NH to the EQ through the boundary at 15°N to be equivalent to the upwelling flux within the NH (+15° to +55°) zone. It is assumed the O present would be advected at the same mass density velocity.

The expression for the mass balance of flux advected from the NH to the upwelling component is described by:

$$\rho_{mean,80-90} * v_{80-90,3ms^{-1}} * A_1 = \rho_{mean,80} * v_{80} * A_2 \quad \text{(D5)}$$

where ρ is mass density, $v_{80-90,3ms^{-1}}$ is the mean horizontal advection velocity from the NH to the EQ, v_{80} is the mean vertical advection velocity at 80 km in the NH, and A_1 and A_2 are the areas associated with the respective regions. It follows that:

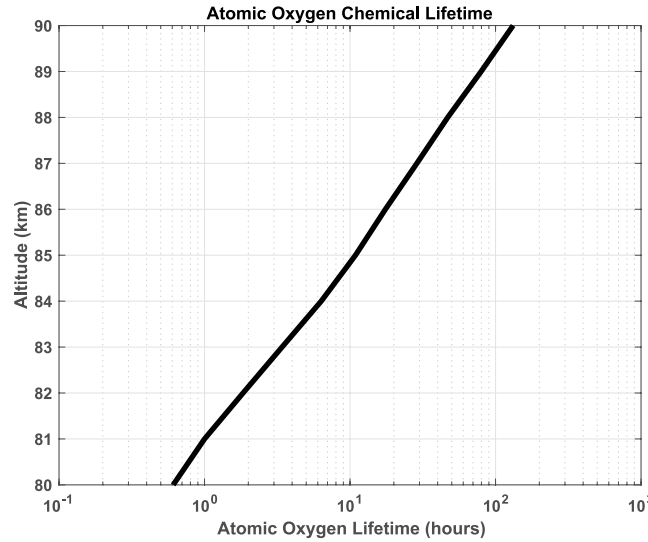

Figure D3. The chemical lifetime, or time it takes the O density to reduce a factor of e at a given altitude, due to it's chemical recombination rate.

$$\upsilon_{80} = \upsilon_{80-90,3ms^{-1}} * (\rho_{mean,80-90}/\rho_{mean,80}) * (A_1/A_2) \quad \text{(D6)}$$

The area of the horizontal cross section of the atmospheric density advected from the NH to the EQ region (A1) is:

$$A_1 = 3.14^*[(r_E + 90)^2 - (r_E + 80)^2] \quad \text{(D7)}$$

where r_E is the Earth radius (in km). The A_1 area is 4.1 10^5 km^2. The NH surface area, A_2, is determined by spherical geometry for 15°–55° to be 1.25 10^8 km^2 which results in A1/A2 = 0.0033. The NRLMSIS 2.0 model was used to determine the mass density ratio at 40°N at summer solstice, that is,

$$\rho_{mean,80-90}/\rho_{mean,80} = 0.42 \quad \text{(D8)}$$

The calculated vertical advection velocity, incorporating the 3 m s^{-1} horizontal velocity at the boundary of the NH and EQ (Equation D6) results in a upwelling of 0.4 cm s^{-1} at 80 km.

The vertical diffusion velocity at 85 km is 13 cm s^{-1} (see Figure D1), a factor of 33 larger than the advection velocity at 80 km. Moreover,the chemical lifetime of O (Figure D3) is ∼1 hr at 80 km and 10 hr at 85 km. The vertical velocity at 80 km penetrates ∼15 m above 80 km during the 1 hr chemical lifetime. Since O density is chemically destroyed for longer periods, we conclude the vertical advection of O due to the residual circulation below 90 km has a negligible contribution to the vertical distribution of O density and the k_{zz} values determined herein.

The component of residual circulation above 95 km associated with the reversal of the zonal flow in the region 95–110 km was investigated and discussed by Qian and Yue (2017). This component of residual circulation indeed affects the coupling of O density with the thermosphere which is discussed in the manuscript Section 5.2.

Appendix D4: The Determination of Horizontal Advection in the NH Zone

We estimate the "contamination" of a zone due to horizonal advection by calculating the fraction a given zone is compromised from the adjacent zone, with meridional velocities described above (3 m s^{-1}). We determine the fraction of the zone compromised, for the chemical recombination lifetime. We assume contamination of a given zone is 50% for the advected fraction, and 0% for the remaining fraction, which varies with altitude. At 85 km, the translation at summer solstice (conditions of AO maximum), the advection penetration from the NH to the EQ for 10 hr (the chemical lifetime) is ∼1°. That penetration into the EQ zone (±15°) is equal to the invasion

Latitude band	Altitude (km)	Meridional Velocity (m s^{-1}), + N	Reference ***
60° N *	80 90	0 -5	2, Fig 9 2, Fig 9
35-40° N *	80 80 80 85 90 90 92 95	-5 -3 to -5, v -4 -3 to +3, v, -5, -5 -5 -5	2, Fig 10 3, Fig 6 1, Fig 6 3, Fig 6 3, Fig 6 2, Fig 10 1, Fig 6 3, Fig 6
15° N*	80 85	-3 -2.5	3, Fig 6 3, Fig 6
Equator **	80 80 85 85 90 90 95 95	+2 to -5, v SAO 15 +5 to -5, v SAO 15 +5 to -5, v SAO 10 +5 to -3, v SAO 7	4 3, Fig 6 4 3, Fig 6 4 3 Fig 6 4 3, Fig 6

*The values represent the AO amplitudes, where v=variable.
** The values represent the annual range and SAO amplitude.
***1=Portnyagin, 1986
2=Portnyagin and Solovjova, 1997
3=Portnyagin and Solovjova, 2000
4=Vincent, 1993

Figure D4. Climatological meridional winds in the 80–96 km altitude region.

fraction/total zone, or 1°/30° (or 3.3%). Given the argument of 50% contamination of the 3.3%, the uncertainty due to horizontal advection, in this case, is 1.7%. The 1.7% contamination from horizontal advection and 1.7% from vertical advection can be statistically summed as root-sum-square, for a total uncertainty of 3.1%.

At higher altitudes (95 km), the chemical lifetimes are long (10s of days) where the diffusion times (Figure D2) are considered for advection. In the EQ zone during spring equinox, the diffusion time is ∼4 days. A 3 m s^{-1} meridional advection velocity contaminates ∼10° of the EQ zone, affecting 33% the EQ zone (±15°. Considering a 50% contamination of the advected fraction, the effective contamination is 16.5%.

The summary of the findings in Appendix D is given in Section 5.2.

Data Availability Statement

The authors thank ESA for providing the SCIAMACHY data within the Cat-1 project 2515. The SCIAMACHY used in this study are available at https://doi.org/10.13012/B2IDB-9526770_V1. The SABER atomic oxygen data used in this study is available at https://doi.org/10.13012/B2IDB-6186460_V1. SABER NetCDF files of updated OH volume emission rates, atomic hydrogen, and other related parameters are available for 2002–2019 at https://cmr.earthdata.nasa.gov/search/concepts/C1214613791-SCIOPS.html.

Acknowledgments
The support for F. Vargas and partial for G. Swenson were provided by the NSF AGS 17-59573 and NSF AGS 11-10334 grants. F. Vargas was also partially supported by NSF grant 19-03336. Support for M. Jones Jr. was from NASA Early Career Investigator (NNH18ZDA001N-ECIP/18-ECIP_2–0018) Programs. The authors thank the reviewers for their comments and suggestions to improve the manuscript.

References

Becker, E., Grygalashvyly, M., & Sonnemann, G. (2020). Gravity wave mixing effects on the OH*-layer. *Advances in Space Research*, *65*(1), 175–188. https://doi.org/10.1016/j.asr.2019.09.043

Becker, E., & von Savigny, C. (2010). Dynamical heating of the polar summer mesopause induced by solar proton events. *Journal of Geophysical Research: Atmospheres*, *115*(D1). https://doi.org/10.1029/2009jd012561

Bovensmann, H., Burrows, J. P., Buchwitz, M., Frerick, J., Noël, S., Rozanov, V. V., et al. (1999). SCIAMACHY: Mission objectives and measurement modes. *Journal of the Atmospheric Sciences*, *562*(2), 127–150.

Chen, Q., Kaufmann, M., Zhu, Y., Liu, J., Koppmann, R., & Riese, M. (2019). Global nighttime atomic oxygen abundances from GOMOS hydroxyl airglow measurements in the mesopause region. *Atmospheric Chemistry and Physics*, *19*(22), 13891–13910. https://doi.org/10.5194/acp-19-13891-2019

Colegrove, F. D., Hanson, W. B., & Johnson, F. S. (1965). Eddy diffusion and oxygen transport in the lower thermosphere. *Journal of Geophysical Research*, *70*(19), 4931–4941. https://doi.org/10.1029/jz070i019p04931

Colegrove, F. D., Johnson, F. S., & Hanson, W. B. (1966). Atmospheric composition in the lower thermosphere. *Journal of Geophysical Research*, *71*(9), 2227–2236. https://doi.org/10.1029/jz071i009p02227

Dunkerton, T. J. (1982). Stochastic parameterization of gravity wave stresses. *Journal of the Atmospheric Sciences*, *39*(8), 1711–1725. https://doi.org/10.1175/1520-0469(1982)039<1711:spogws>2.0.co;2

Emmert, J. T., Drob, D. P., Picone, J. M., Siskind, D. E., Jones, M., Jr., Mlynczak, M. G., et al. (2021). NRLMSIS 2.0: A whole-atmosphere empirical model of temperature and neutral species densities. *Earth and Space Science*, *8*(3), e2020EA001321.

Frederick, J. E., & Hudson, R. D. (1980). Dissociation of molecular oxygen in the Schumann-Runge Bands. *Journal of the Atmospheric Sciences*, *37*(5), 1099–1106. https://doi.org/10.1175/1520-0469(1980)037<1099:domoit>2.0.co;2

Fritts, D. C., & Alexander, M. J. (2003). Gravity wave dynamics and effects in the middle atmosphere. *Reviews of Geophysics*, *41*(1). https://doi.org/10.1029/2001rg000106

Fuller-Rowell, T. J. (1998). The "Thermospheric Spoon": A mechanism for the semiannual density variation. *Journal of Geophysical Research: Space Physics*, *103*(A3), 3951–3956. https://doi.org/10.1029/97ja03335

Garcia, R. R., Dunkerton, T. J., Lieberman, R. S., & Vincent, R. A. (1997). Climatology of the semiannual oscillation of the tropical middle atmosphere. *Journal of Geophysical Research*, *102*(D22), 26019–26032.

Garcia, R. R., Marsh, D. R., Kinnison, D. E., Boville, B. A., & Sassi, F. (2007). Simulation of secular trends in the middle atmosphere, 1950–2003. *Journal of Geophysical Research*, *112*(D9). https://doi.org/10.1029/2006jd007485

Garcia, R. R., & Solomon, S. (1985). The effect of breaking gravity waves on the dynamics and chemical composition of the mesosphere and lower thermosphere. *Journal of Geophysical Research: Atmospheres*, *90*(D2), 3850–3868.

Gardner, C. S. (2018). Role of wave-induced diffusion and energy flux in the vertical transport of atmospheric constituents in the mesopause region. *Journal of Geophysical Research*, *123*(12), 6581–6604. https://doi.org/10.1029/2018jd028359

Gardner, C. S., Chu, X., Espy, P. J., Plane, J. M. C., Marsh, D. R., & Janches, D. (2011). Seasonal variations of the mesospheric Fe layer at Rothera, Antarctica (67.5°S, 68.0°W). *Journal of Geophysical Research*, *116*(D2). https://doi.org/10.1029/2010jd014655

Grygalashvyly, M., Becker, E., & Sonnemann, G. R. (2012). Gravity wave mixing and effective diffusivity for minor chemical constituents in the mesosphere/lower thermosphere. *Space Science Reviews*, *168*(1), 333–362. https://doi.org/10.1007/s11214-011-9857-x

Guo, L., & Lehmacher, G. (2009). First meteor radar observations of tidal oscillations over Jicamarca (11.95°S, 76.87°W). *Annales Geophysicae*, *27*(6), 2575–2583.

Hines, C. O. (1960). Internal atmospheric gravity waves at ionospheric heights. *Canadian Journal of Physics*, *38*(11), 1441–1481. https://doi.org/10.1139/p60-150

Hirota, I. (1978). Equatorial waves in the upper stratosphere and mesosphere in relation to the semiannual oscillation of the zonal wind. *Journal of the Atmospheric Sciences*, *35*(4), 714–722. https://doi.org/10.1175/1520-0469(1978)035<0714:ewitus>2.0.co;2

Jacchia, L. G. (1964). *Static diffusion models of the upper atmosphere with Empirical temperature profiles* (p. 170). SAO Special Report.

Jacchia, L. G. (1970). *New static models of the thermosphere and Exosphere with Empirical temperature profiles* (p. 313). SAO Special Report.

Jones, M., Emmert, J. T., Drob, D. P., Picone, J. M., & Meier, R. R. (2018). Origins of the thermosphere-ionosphere semiannual oscillation: Reformulating the "Thermospheric Spoon" mechanism. *Journal of Geophysical Research: Space Physics*, *123*(1), 931–954. https://doi.org/10.1002/2017ja024861

Jones, M., Emmert, J. T., Drob, D. P., & Siskind, D. E. (2017). Middle atmosphere dynamical sources of the semiannual oscillation in the thermosphere and ionosphere. *Geophysical Research Letters*, *44*(1), 12–21. https://doi.org/10.1002/2016gl071741

Jones, M., Forbes, J. M., & Hagan, M. E. (2014). Tidal-induced net transport effects on the oxygen distribution in the thermosphere. *Geophysical Research Letters*, *41*(14), 5272–5279. https://doi.org/10.1002/2014gl060698

Jones, M., Jr., Sutton, E. K., Emmert, J. T., Siskind, D. E., & Drob, D. P. (2021). On the effects of mesospheric and lower thermospheric oxygen chemistry on the thermosphere and ionosphere semiannual oscillation. *Journal of Geophysical Research: Space Physics*, *126*(3), e2020JA028647.

Kaufmann, M., Zhu, Y., Ern, M., & Riese, M. (2014). Global distribution of atomic oxygen in the mesopause region as derived from SCIAMACHY O(^{1}S) green line measurements. *Geophysical Research Letters*, *41*(17), 6274–6280. https://doi.org/10.1002/2014gl060574

Koppers, G., & Murtagh, D. (1996). Model studies of the influence of O_2 photodissociation parameterizations in the Schumann-Runge bands on ozone related photolysis in the upper atmosphere. *Annales Geophysicae*, *14*, 68–79. https://doi.org/10.1007/s00585-996-0068-9

Lednyts'kyy, O., von Savigny, C., & Weber, M. (2017). Sensitivity of equatorial atomic oxygen in the MLT region to the 11-year and 27-day solar cycles. *Journal of Atmospheric and Solar-Terrestrial Physics*, *162*, 136–150.

Li, F., Liu, A. Z., & Swenson, G. R. (2005). Characteristics of instabilities in the mesopause region over Maui, Hawaii. *Journal of Geophysical Research*, *110*(D9). https://doi.org/10.1029/2004jd005097

Liu, A. Z. (2009). Estimate eddy diffusion coefficients from gravity wave vertical momentum and heat fluxes. *Geophysical Research Letters*, *36*(8). https://doi.org/10.1029/2009gl037495

Liu, A. Z., Guo, Y. F., Vargas, F., & Swenson, G. R. (2016). First measurement of horizontal wind and temperature in the lower thermosphere (105–140 km) with Na lidar at Andes Lidar Observatory. *Geophysical Research Letters*, *43*, 2374–2380. https://doi.org/10.1002/2016gl068461

Liu, H.-L., Bardeen, C. G., Foster, B. T., Lauritzen, P., Liu, J., Lu, G., et al. (2018). Development and validation of the whole atmosphere community climate model with thermosphere and ionosphere extension (WACCM-X 2.0). *Journal of Advances in Modeling Earth Systems*, *10*(2), 381–402. https://doi.org/10.1002/2017ms001232

Lübken, F.-J. (1997). Seasonal variation of turbulent energy dissipation rates at high latitudes as determined by in-situ measurements of neutral density fluctuations. *Journal of Geophysical Research: Atmospheres*, *102*(D12), 13441–13456. https://doi.org/10.1029/97jd00853

Malhotra, G., Ridley, A. J., Marsh, D. R., Wu, C., Paxton, L. J., & Mlynczak, M. G. (2020). Impacts of lower thermospheric atomic oxygen on thermospheric dynamics and composition using the Global Ionosphere Thermosphere model. *Journal of Geophysical Research: Space Physics*, *125*(9), e2020JA027877.

Mast, J., Mlynczak, M. G., Hunt, L. A., Marshall, B. T., Mertens, C. J., Russell, J. M., III, et al. (2013). Absolute concentrations of highly vibrationally excited OH(v = 9 + 8) in the mesopause region derived from the TIMED/SABER instrument. *Geophysical Research Letters*, *40*(3), 646–650.

Mauldin, L. E., III, Zaun, N. H. M. P. M., Jr., Guy, J. H., Vaughn, W. R., & Vaughn, W. R. (1985). Stratospheric aerosol and gas experiment II instrument: A functional description. *Optical Engineering*, *24*(2), 307–312. https://doi.org/10.1117/12.797347310.1117/12.7973473

Mlynczak, M. G., Hunt, L. A., Mast, J. C., Thomas Marshall, B., Russell, J. M., III, Smith, A. K., et al. (2013). Atomic oxygen in the mesosphere and lower thermosphere derived from SABER: Algorithm theoretical basis and measurement uncertainty. *Journal of Geophysical Research: Atmospheres*, *118*(11), 5724–5735.

Mlynczak, M. G., Hunt, L. A., Russell, J. M., III, & Marshall, B. T. (2018). Updated SABER night atomic oxygen and implications for SABER ozone and atomic hydrogen. *Geophysical Research Letters*, *45*(11), 5735–5741.

Picone, J., Lean, J., Jones, M., & Meier, R. (2019). On the latitudinal variation of the semiannual oscillation in received solar radiation and temperature. *Journal of Atmospheric and Solar-Terrestrial Physics*, *194*, 105098.

Portnyagin, Y. (1986). The climatic wind regime in the lower thermosphere from meteor radar observations. *Journal of Atmospheric and Solar-Terrestrial Physics*, *48*, 1099–1109. https://doi.org/10.1016/0021-9169(86)90030-9

Portnyagin, Y., & Solovjeva, T. (1997). The role of vertical momentum fluxes in maintaining global meridional circulation in the lower thermosphere/upper mesosphere. *Journal of Atmospheric and Solar-Terrestrial Physics*, *59*(5), 511–525.

Portnyagin, Y. I., & Solovjova, T. V. (2000). Global empirical wind model for the upper mesosphere/lower thermosphere. I. Prevailing wind. *Annales Geophysicae*, *18*(3), 300–315.

Qian, L., Burns, A. G., Solomon, S. C., & Wang, W. (2013). Annual/semiannual variation of the ionosphere. *Geophysical Research Letters*, *40*(10), 1928–1933. https://doi.org/10.1002/grl.50448

Qian, L., Solomon, S. C., & Kane, T. J. (2009). Seasonal variation of thermospheric density and composition. *Journal of Geophysical Research: Space Physics*, *114*(A1). https://doi.org/10.1029/2008ja013643

Qian, L., & Yue, J. (2017). Impact of the lower thermospheric winter-to-summer residual circulation on thermospheric composition. *Geophysical Research Letters*, *44*(9), 3971–3979.

Russell, J. M., Mlynczak, M. G., Gordley, L. L., Tansock, J. J., & Esplin, R. W. (1999). Overview of the SABER experiment and preliminary calibration results. *Proceeding of SPIE 3756, Optical Spectroscopic Techniques and Instrumentation for atmospheric and space Research III*. https://doi.org/10.1117/12.366382

Salinas, C. C. J. H., Chang, L. C., Liang, M.-C., Yue, J., Russell, J., & Mlynczak, M. (2016). Impacts of SABER CO_2-based eddy diffusion coefficients in the lower thermosphere on the ionosphere/thermosphere. *Journal of Geophysical Research: Space Physics*, *121*(12), 12092. https://doi.org/10.1002/2016ja023161

Sander, S. P., Golden, D. M., Kurylo, M. J., Moortgat, G. K., Wine, P. H., Ravishankara, A. R., & Orkin, V. L. (2011). Chemical kinetics and photochemical data for use in Atmospheric Studies Evaluation Number 15. *JPL Publication*, *10*(6).

Smith, A. K., Marsh, D. R., Mlynczak, M. G., & Mast, J. C. (2010). Temporal variations of atomic oxygen in the upper mesosphere from SABER. *Journal of Geophysical Research: Atmospheres*, *115*(D18). https://doi.org/10.1029/2009jd013434

Swenson, G., Salinas, C. C. J. H., Vargas, F., Zhu, Y., Kaufmann, M., Jones, M., Jr., et al. (2019). Determination of global mean eddy diffusive transport in the mesosphere and lower thermosphere from atomic oxygen and carbon dioxide climatologies. *Journal of Geophysical Research: Atmospheres*, *124*(23), 13519–13533. https://doi.org/10.1029/2019jd031329

Swenson, G., Yee, Y., Vargas, F., & Liu, A. (2018). Vertical diffusion transport of atomic oxygen in the mesopause region consistent with chemical losses and continuity: Global mean and inter-annual variability. *Journal of Atmospheric and Solar-Terrestrial Physics*, *178*, 47–57. https://doi.org/10.1016/j.jastp.2018.05.014

Tian, C., Hu, X., Liu, A. Z., Yan, Z., Xu, Q., Cai, B., & Yang, J. (2021). Diurnal and seasonal variability of short-period gravity waves at 40 degrees N using meteor radar wind observations. *Advances in Space Research*.

Vincent, R. (1993). Long-period motions in the equatorial mesosphere. *Journal of Atmospheric and Solar-Terrestrial Physics*, *55*, 1067–1080. https://doi.org/10.1016/0021-9169(93)90098-j

Yue, J., Jian, Y., Wang, W., Meier, R., Burns, A., Qian, L., & Mlynczak, M. (2019). Annual and semiannual oscillations of thermospheric composition in TIMED/GUVI limb measurements. *Journal of Geophysical Research: Space Physics*, *124*(4), 3067–3082.

Zhu, Y., & Kaufmann, M. (2018). Atomic oxygen abundance retrieved from SCIAMACHY hydroxyl nightglow measurements. *Geophysical Research Letters*, *45*(17), 9314–9322. https://doi.org/10.1029/2018gl079259

Zhu, Y., Kaufmann, M., Ern, M., & Riese, M. (2015). Nighttime atomic oxygen in the mesopause region retrieved from SCIAMACHY O(^{1}S) green line measurements and its response to solar cycle variation. *Journal of Geophysical Research: Space Physics*, *120*(10), 9057–9073. https://doi.org/10.1002/2015ja021405